Title: Cell-supracellular structural relations solve the French Flag Problem without graded molecular control

Authors: Clint S. Ko[1,3], Ruonan Chen[1,3], Nina T. Magid[1], Katharine Courtemanche[1], Pearson W. Miller[2]*, Alan R. Rodrigues[1,4]*, Amy E. Shyer[1,4]*

Affiliations:

[1]Laboratory of Morphogenesis, The Rockefeller University; New York, NY 10065

[2]Department of Mathematics, UC San Diego; La Jolla, CA 92093

[3]First authors

[4]These authors contributed equally to this work

*Corresponding author. Email: ashyer@rockefeller.edu, arodrigues@rockefeller.edu, pwmiller@ucsd.edu

Abstract: The molecular characterization of tissue organization through spatial omics brings renewed attention to the issue, formulated in Wolpert's French Flag, of how spatial patterns of cell state emerge. Here, we address the skeletal pattern of adjacent cartilage and soft tissue. We find that cellular and supracellular structures are co-constitutive and result in cell-ECM and cell-cell-based structures that canalize cartilage and soft tissue fate, respectively. A bistability in these fate-setting structures establishes pattern length scale and is sufficient to break symmetry in the mesenchyme. However, an adjacent epithelium, through signals like Wnt, can locally seed the bistability to ensure the epithelial-adjacency of soft tissue. Rather than acting in a graded manner to provide positional information, Wnt affects cell fate by promoting a supracellular structure. Together, these results support a solution to the French Flag problem where fate pattern originates through structural relations between cell and supracellular levels.

Introduction

The rapidly expanding suite of spatial omics tools and related image analysis methods have revealed associated patterns of molecular expression and tissue structure in disease states and aging[1,2,3]. The increasing abundance of characterizations that link patterns across length scales underscores the need to consider the causal relationships across these levels of organization. Furthermore, a mechanistic understanding of how patterns of cell states and tissue structure co-emerge is essential for effective therapeutic intervention. In such contexts, understanding of causal relationships continues to be guided by classical models like Lewis Wolpert's French Flag[4,5], where differences in signaling molecule concentration generate subcellular positional information across a tissue, which then templates the corresponding structures[6,7,8,9,10,11]. Here, we identify a novel mechanism for the organization of compartments within a tissue that does not rely on graded molecular control. Instead, we find that fate patterns originate through structural relations between cell and supracellular levels of organization.

In complex systems like organs, the structures that form and the potential for such structures to reciprocally adapt in response to relations within and across levels (cell, supracellular, organ, etc.) enable organizing processes that are unique to biology. Such adaptive and reciprocally causal relationships are specific to living systems because they stem from evolutionary processes fueled by adaptation and, therefore, may not be simply derivable from physical or chemical first principles[12,13,14]. For example, unlike living systems, water molecules do not fundamentally change within a snowflake as it forms, nor do Lego blocks transform as they are incorporated into a structure. However, cells can adapt in response to the structures they build[15,16,17]. Along these lines, while physical and chemical principles and tools are fundamental for studying living systems, as exemplified by the power of mechanochemical frameworks[18,19,20,21,22,23], additional principles may be necessary to fully capture certain aspects of living systems.

A framing of tissues through concepts from ecology, in particular a focus on the mutual and often simultaneous relations of structures across scales and the associated organization, may be a powerful complement to current mechanochemical frameworks[24,25]. Much in the way that ecologists must be attuned to the adaptive behavior that occurs through reciprocal relations within and across the hierarchy of levels of organization, there is an increasing need to examine the "ecology" within tissues in organs. While the aspects of living systems that set them apart from inorganic systems have been theoretically considered[26,27,28], empirical examples are still limited. Without clear and concrete illustrations of the particular nature of the structures and organizing processes across levels in organs, our ability to grasp causality in health and disease and therefore successfully intervene may be limited.

Here, we bring an ecological perspective to the patterning of the skeleton that emerges in the developing limb, a well-studied compartmentalization process where the mechanism of symmetry-breaking remains incomplete despite investigations through molecular as well as cellular and mechanical perspectives[29,30,31,32]. This pattern first emerges as adjacent compartments of cartilage and soft tissue in the mesenchymal cell population of the limb bud, which is encased by an epithelium called the ectoderm. Adopting an ecological perspective requires tools that allow for the study of evolving structures and their causal relations across levels during the initiation of cellular differentiation spatial patterns. To that end, we developed a new *ex vivo* platform, termed organite, using primary progenitor cells from the embryonic chicken limb epithelial and mesenchymal tissues. The organite platform recreates the limb tissue

ecosystem and captures the process whereby a field of homogenous progenitor cells compartmentalizes into cartilage and soft tissue in the presence of secretory epithelial tissue.

Combining the organite assay with both static and live-cell imaging allowed us to discover that both cartilage and soft tissue fate are triggered by distinct supracellular structures that are generated from within each collective, rather than from an external boundary, microenvironment, or substrate. We discover that such a top-down cue can be generated from within through an inter-level dynamic where cell relations and supracellular structures are mutually constitutive. Using experiment and mathematical modeling, we determine that the mesenchyme is structurally bistable and can self-compartmentalize into cartilage and soft tissue fates through relations at the cell and supracellular level. Appreciating the co-constituting nature of cell and supracellular level structures allowed us to present a new role for signaling molecules from the epithelium, where they act through this co-constitution to bias the structural bistability in the neighboring mesenchyme. Together, these findings present a new mechanism for the self-organization of fates across a tissue that depends upon the unique way structures relate across levels in biology, rather than the graded control of signaling molecules.

Reconstitution of tissue compartmentalization in an *ex vivo* primary progenitor cell assay

To investigate the role of structural dynamics in patterns of cellular differentiation, we developed a novel *ex vivo* platform that recapitulates the pattern of cellular differentiation outside of the embryo. Because such compartmentalization is often stimulated by epithelial-mesenchymal interactions[33,34,35], the platform incorporates both mesenchymal and epithelial progenitors from the embryonic chicken limb. Specifically, a dense disc with a particular proportion of dissociated progenitor epithelial (ectodermal) and mesenchymal cells from the embryonic day 4 avian limb bud (Figure 1A) is seeded and allowed to spontaneously arrange into spherical ectodermal tissue surrounded by a field of mesenchyme. After 24 hours of culture, the organite platform reproduced a stereotyped tissue differentiation pattern in the mesenchymal population in which Twist-positive cells, indicative of soft tissue fate[36], formed adjacent to the ectoderm surrounded by a field of Sox9-positive cells, indicative of cartilage fate[37] (Figures 1A-1B). This arrangement of compartments recapitulated the basic fate pattern that emerges within the limb bud (Figure S1A), though in an inverted geometry.

We named this class of *ex vivo* reconstitutions “organite” in reference to utilizing cells that are residents of the developing organ. Therefore, a strength of the platform is featuring primary progenitor cells, which are the cells that establish tissue organization within organs initially, as compared to adult stem cells, which are charged with regeneration. The inclusion of progenitors from both tissue types dispenses with the need to supplement with exogenous matrix to mimic the mesenchyme or add exogenous differentiation cues in lieu of the epithelium. Further, because both tissues are dissociated and, therefore, any molecular prepattern or template is reset, the system captures the pattern from its inception.

In addition to recapitulating cell fate pattern, we observed structural features at the cell and supracellular scale that are specific to each compartment. With respect to cell arrangement, we find that cell density is elevated in the soft tissue domain, which was associated with highly anisotropic cell shapes in the organite, suggesting that cell elongation and packing are principal features of how the soft tissue compartment is organized (Figures 1A-1D). Indeed, we found that the cell-cell adhesion molecule N-cadherin (Ncad), associated with cartilage formation at subsequent stages[38], was present at high levels specific to the densely packed soft tissue zone, indicating a role for cell-cell adhesion in this packed supracellular structure (Figure 1E). Next,

with respect to extracellular matrix organization, we observed a dense network of fibronectin fibers in the cartilage domain and a lack of fibronectin in soft tissue (Figures 1E -1F). We assayed for these structural hallmarks in the limb bud and observed a similar pattern with respect to cell density and matrix organization specific to each domain *in vivo*[39,40] (Figures S1A-S1B). Therefore, the organite system recapitulates essential aspects of cell fate as well as cell and supracellular structural organization during skeletal pattern formation.

To elucidate the development of such structural patterns, we performed live-cell imaging of organite culture supplemented with fluorescently-tagged fibronectin antibody. In early phases (0-9 hrs) of organite culture, fibronectin is expressed and produced by the ectoderm[41] and across the mesenchyme (Figures 1G, S1C, and Movie S1), rather than being initially restricted near the ectoderm in the forming soft tissue zone. Strikingly, after approximately 10 hrs, we observed an outward flow of fibronectin away from the ectoderm and forming soft tissue (Figure 1H and Movie S2), producing a fibronectin clearing specific to the soft tissue zone and a fibronectin-cell network specific to the cartilage zone. Thus, organite culture revealed emergent supracellular structural dynamics spatiotemporally linked to the process of compartmentalization. Motivated by these observations of structural dynamics in the organite, previously precluded *in vivo* by the geometry of the limb bud, we investigated whether such supracellular structures are a cause rather than a consequence of cell fate pattern.

Intrinsically generated cell-ECM supracellular structure is the cue for cartilage fate

We explored whether structures at the supracellular scale are the yet-to-be-identified cue for Sox9 expression to activate cartilage fate. Suggestive of a requirement for such a structure, in an *ex vivo* model comprised solely of limb mesenchymal progenitor cells, we found that the majority of cells will activate Sox9, but only above a particular threshold of cell density (Figures 2A-2B). We found that in such dense collectives, cell-ECM-based interactions mediate collective organization, with cells developing an increasingly dense fibronectin network over time (Figure 2C and Movie S3). Further, we observed that focal adhesions, marked by paxillin, vinculin, and β1 integrin, were enriched at the interfaces between cells, similar to stitch adhesions[42] (Figures 2D and S2A). Disruption of such adhesions with a focal adhesion kinase inhibitor (FAKi) resulted in the expected absence of a fibronectin network, loss of paxillin enrichment at cell interfaces, and a decrease in linkages between cells (Figures 2E, 2F, and S2B). Importantly, FAKi treatment also resulted in a significant reduction in Sox9 expression. These results indicate that cells form an ECM-based supracellular structure and that this supracellular structure is necessary for the activation of Sox9 in the cells within the collective, evidencing a role for "top-down" causation from the supracellular to the cellular level[43,44].

Of note, this supracellular cue comes from within the collective as opposed to a microenvironment, substrate, or boundary, as is predominantly the case for top-down cues[45,46,47,48]. Therefore, we next sought to determine how the formation of the particular cell-ECM network structure needed to activate Sox9 is organized from within. We posited that, in the absence of an external evocator, structural relations across levels of organization (cell and supracellular) within the collective could serve as a form of "internal organizer". Specifically, just as cells engage with ECM to guide supracellular structure (e.g. a cell-ECM network), this supracellular structure may guide the way cells relate to the ECM by promoting further cell-ECM engagement or ECM production. Such an inter-level reciprocal constitution would be capable of fueling and regulating the formation of a supracellular structure from within, but would require a means for individual cells to sense and respond to their structural context. We

hypothesized a role for Ca^{2+} signaling given known roles in regulating cell-ECM sensing[49,50]. Indeed, we observe a reduction of Sox9 activation upon inhibition of calmodulin, a key downstream effector in intracellular calcium signaling[51] (Figure S2C).

To more specifically test the hypothesis that cells canalize cartilage fate by utilizing Ca^{2+} signaling to increase cell-ECM relations in response to the emerging supracellular cell-ECM structure, we focused on the TRPV4 Ca^{2+}-permeable cation channel, a channel with sensitivity to structural stimuli[52,53] and associations with cartilage formation[54,55,56]. Pharmacological inhibition of TRPV4 reduced fibronectin and paxillin levels, weakened supracellular connectivity, and consequently inhibited Sox9 expression (Figures 2G, 2H, and S2B). These results indicate that cells require TRPV4-based sensing of the structural context to relate to the ECM and form the supracellular structural cue for Sox9. To test whether activation of Sox9 through focal adhesions is mediated through TRPV4 activity, we activated TRPV4 in cells treated with FAKi. We found that fibronectin and paxillin levels, tight cell associations, and Sox9 expression are rescued (Figure 2G-2H). These results indicate that Ca^{2+} signaling through TRPV4 is sufficient for cell-ECM engagement, allowing individual cells to engage with surrounding ECM in response to structural changes. Such signaling is a means for inter-level reciprocal constitution, where the relations between cell and supracellular scales fuel the self-organization of the top-down structural cue (cell-ECM network) needed for Sox9 activation and cartilage fate.

Lastly, in considering what mediates the effect of the cell-ECM supracellular cue on Sox9 activation, we posited a role for cytoskeletal structure. In line with this hypothesis, alterations in Ca^{2+} signaling or focal adhesions led to changes in actin network architecture and cell shape[57,58] (Figures 2E, 2G, and S2B). Further, a diffuse, rather than bundled, stress fiber arrangement of actin fibers is associated with Sox9 activation, both *in vivo* and *ex vivo* (Figures 2I and Fig. S2D). Lastly, previous studies have described an association between cytoskeletal organization and Sox9[59]. Upon disruption of stress fibers through Rho-associated protein kinase (ROCK) inhibition (Y27632), limb progenitors activated widespread Sox9 expression even at lower cell densities not normally capable of such widespread expression (Figures 2J-2K). Notably, Sox9 activation occurred in spite of the fact that Y27632 treatment led to decreased focal adhesions and loss of the fibronectin network (Figure 2L). Further, Y27632 treatment rescued Sox9 when TRPV4 was inhibited, despite exhibiting the lowest levels of fibronectin and paxillin (Figure 2L). The activation of Sox9 expression by ectopic manipulation of cytoskeletal architecture in the absence of stable focal adhesions and fibronectin network formation indicates that cytoskeletal organization is a key and sufficient structural feature. Our findings contextualize results from decades ago, suggesting that if single cells *in vitro* adopt the proper architecture, they can become cartilage in culture[60,61]. Here, we show that cytoskeletal architecture is organized through an intrinsically generated supracellular cell-ECM structure (Figure 2M). Our results suggest that, in a native tissue context, a cell-ECM-based supracellular structure guides cytoskeletal architecture toward the conformation necessary for Sox9 activation, dispensing with the need for a molecular ligand to activate Sox9 in the cartilage zone.

Epithelial Wnt activates soft tissue fate through cell-cell-based supracellular structure

The establishment of skeletal pattern depends upon restricting cartilage fate (marked by Sox9 expression) to the core of the limb bud and enabling soft tissue (marked by Twist expression) near the ectoderm. Ectodermal signals are understood to organize such mesenchymal patterns by acting in a concentration-dependent manner to transcriptionally activate and repress Twist and Sox9 in each cell over a particular distance[36,62]. The shape of the gradient would set the distance,

and the signaling molecule would, through gene regulation, determine fate. Given our discovery of a supracellular cue for cartilage fate, we investigated whether, instead, ectodermal signals affect fate markers through changes in supracellular structure. Treatment with the key ectodermal signal Wnt (Wnt3a)[62,63] recapitulates the ectoderm's repression of Sox9 in *ex vivo* cultures of limb mesenchymal cells (Figures 3A-3B). Of note, we observe that Wnt treatment also results in reduced fibronectin and paxillin, indicative of a disrupted cell-ECM supracellular structure (Figures 3A, S3A, and S3B). When we increased cell-ECM engagement by treating with the TRPV4 channel activator, paxillin levels are rescued, and Wnt is not able to repress Sox9 expression (Figures 3A-3B). Through live-cell imaging, we observed that Wnt treatment resulted in a heterogeneous fibronectin network of low fibronectin levels interspersed with denser fibronectin clusters (Figure S3C and Movies S4 and S5). Additionally, even when cultures were supplemented with excess fibronectin, Wnt-treated cultures develop a reduced network relative to control cultures (Figures 3C -3D), further indicating that Wnt treatment reduces cell-ECM engagement to affect supracellular structure. All together, these results are consistent with our hypothesis that the inhibitory effect of Wnt on Sox9 occurs through suppression of a cell-ECM-based supracellular structure.

In addition to repressing Sox9, Wnt treatment led to an increase in expression of the soft tissue marker Twist (Figures 3E-3F). Consistent with our organite observations (Figure 1E), these Twist-positive aggregations are also enriched for Ncad, indicating that, in lieu of cell-ECM engagement, Wnt induces a shift toward cell-cell-based adhesion (Figure 3E and S3D). When we treated cultures with a competitive inhibitor of Ncad in the presence of Wnt, cell packing and Twist expression were suppressed (Figures 3E-3F). These results indicate that Wnt, rather than acting through direct transcriptional regulation, enables soft tissue fate through increasing cell-cell relations in lieu of cell-ECM engagement (Figure 3G).

However, we found that Ncad levels upon Wnt treatment increased non-linearly with cell density (Figures 3H-3I), suggesting that Wnt does not meaningfully increase Ncad levels in individual isolated cells, but can enable increases in Ncad levels in high cell density contexts. Consistent with these findings, we observe that Wnt is only able to induce Twist in the most packed regions of high-density cultures (Figures 3E, 3J-3K, and S3E). To further test the hypothesis that denser cellular environments enable Wnt to canalize cells towards soft tissue fate by further increasing cell-cell relations, we varied starting cell density in the organite. We observed that increasing density changes the profile of Twist expression, increasing the expression levels across the soft tissue domain (Figures 3L-3M). Given that we compared cultures where ectoderm size and density are similar, the observed increase in Twist occurs under comparable levels of ectodermal signaling cues. Taken together, these results show that the effect of Wnt on repressing cartilage fate and activating soft tissue fate is contingent on a particular supracellular structure. This is because Wnt activates Twist through an inter-level reciprocal constitution in the mesenchyme where cell-cell adhesion enables a dense cell-cell-based supracellular structure, but this supracellular structure also enables further cell-cell adhesion to guide cells toward soft tissue fate (Figure 3G).

A structural bistability drives mesenchymal self-compartmentalization

Our observation of adjacent Twist-positive and Sox9-positive domains in mesenchymal cell-only cultures treated with Wnt (Figure 3J) suggested that dynamics within the mesenchyme are sufficient for self-compartmentalization, perhaps even in the absence of Wnt. Furthermore, higher densities promoted the formation of more prominent Twist-positive clusters, suggesting

that self-compartmentalization is cell density dependent (Figures 3J, 3K, and S3E). Accordingly, we characterized structural dynamics and fate patterning in control and Wnt-treated high-density mesenchymal cell-only cultures, akin to the classic micromass system[64,65,66,67,68,69,70,71]. By 24 hours, we observed a clear bifurcation into Sox9 and Twist positive domains in Wnt-treated cultures, with Twist expression in the densest regions of cultures (Figure 4A). Conversely, control micromass cultures exhibited relatively uniform high Sox9 expression and low Twist expression (Figure 4B). However, observing control cultures for the ensuing 20 hours revealed a clear mutual exclusion of adjacent Twist and Sox9 expressing domains, with Twist expression again in the densest regions (Figure 4B). These results indicated that the mesenchyme has the capacity to self-segregate into soft tissue and cartilage fates, in the absence of the epithelium, and even in the absence of exogenous signals like Wnt.

In both control micromass cultures at 45 hours and Wnt-treated cultures at 24 hours, the segregation of fate temporally coincided with a distinct structural (cell-cell and cell-ECM) pattern (Figures 4A-4B), consistent with a causal link between supracellular structure and fate. Moreover, the pattern of spaced foci of fibronectin centered within dense, Twist-positive cellular aggregates of relatively low fibronectin density in Wnt and control micromass cultures bears a striking resemblance to the arrangement in organite culture (with ectoderm-associated fibronectin resembling the micromass foci) (Figure 4C), though with less regularity. Having evidenced that the cues for Twist and Sox9 activation come from cell-cell and cell-ECM supracellular structures, respectively, we investigated how such structures spontaneously emerge in the micromass without any nucleation from the ectoderm or ectoderm signals. We posited that such structural symmetry-breaking stems from a bistability where cell-cell and cell-ECM regimes are each self-amplifying (through inter-level relations) but mutually antagonistic. Such cell-cell and cell-ECM mutual antagonism was evidenced by the observation that increasing cell-ECM engagement through activation of β1-integrins[72] resulted in lower levels of Ncad and a concomitant decrease in multicellular aggregation necessary for cell-cell engagement in both organite and mesenchymal cell-only culture (Figures 4D-4E, and S4).

To quantitatively explore how such a mechanism could account for structural symmetry-breaking, we developed a continuum mechanical model in which the dynamics of cell commitment are treated as a bistable nonlinear switch. Specifically, local ECM amount and engagement (tension), as well as cell densities, modulate thresholds corresponding to cell-ECM and cell-cell relational modes, respectively. As cells commit to one of these relational modes, that choice is amplified and the other option is diminished based on the supracellular context that cells themselves generate and find themselves within (see Supplemental Material) (Figure 4F). Indeed, our simulations recover the structural dynamics observed in our experiments with control cultures. Specifically, an initially homogenous field of cells that are prone to cell-ECM relations spontaneously aggregates, which, over time, leads to regions of high cell density (Figure 4G). Such dense supracellular structures promote cell-cell adhesion and will self-amplify density through the inter-level reciprocal constitution we identified. Thus, unexpectedly, in control cultures, the cell density needed to trigger a switch to cell-cell relations emerges through spontaneous cell-ECM-based aggregation. Regions that are dense and Twist positive can switch to a cell-cell relational mode despite the central fibronectin foci, because the supracellular cue for cell-ECM engagement requires not just the presence of ECM, but the presence of a tense, engaged ECM network. This is a central feature in our model, supported by our results showing that the soft tissue in the organite relates through cell-cell adhesion even with abundant access to ECM material, with the adjacent ectoderm being a significant ECM source. Such foci are likely a

persistent vestige of initial aggregation via cell-ECM interactions, and not a cue for cell-ECM engagement. Taken together, our theory and experiments indicated that symmetry-breaking of a homogeneous field of cells with a tendency towards cell-ECM engagement relies upon the spontaneous emergence of supracellular structure conducive to a local switch to cell-cell relations.

Our model also confirmed our Wnt-treated micromass results (Figure 4A), where moderately increasing the propensity of all cells to relate through cell-cell-based adhesion, at the expense of cell-ECM engagement, accelerates and exaggerates symmetry-breaking and self-compartmentalization (Figure 4H). Promoting cell-cell adhesion at a lower threshold of cell density through Wnt treatment or in our model lowers the extent of cell-ECM-based aggregation needed, thereby reducing the time to break symmetry. Indeed, with Wnt treatment in micromass cultures, Ncad expression and cell density in aggregates are greatly amplified (Figure 4A). In these cultures, fibronectin foci remain in the center of aggregates with high Ncad and Twist expression, further supporting the notion that these ECM structures are the remnant of an ECM-based route to aggregation, rather than reflective of continued local cell-ECM engagement. Altogether, our experimental results and model demonstrate that mesenchymal supracellular structure is bistable because cell-cell and cell-ECM relational regimes each self-amplify but are mutually opposed. This bistability enables the mesenchyme to self-compartmentalize while remaining open to input from signals like Wnt, which increase the competency for symmetry breaking even in the absence of spatial localization.

Wnt spatially orients skeletal patterning without graded control

Given that signals from the epithelium are not required to break symmetry in the mesenchyme but can contribute to symmetry-breaking mesenchymal dynamics, we investigated how epithelial signals participate in proper skeletal pattern. To do so, we adapted our continuum mechanical model to organite culture by including a region of epithelial tissue that biases cells to engage in cell-cell adhesion. Our model indicates that biasing cells towards cell-cell-based supracellular structure near the ectoderm leads the local ECM to recede toward the emerging cartilage zone, where cell-ECM engagement is high and self-amplifying (Figure 5A). A shift from ECM engagement to cell-cell adhesion adjacent to the ectoderm leads to an increase in cell packing, which guides cells further away from the ectoderm towards increased cell-cell adhesion. Therefore, in the context of localized signals from the epithelium, the mesenchymal bistability can play out in a spatially stereotyped manner.

Notably, localizing Wnt influence solely at the ectoderm, rather than extending into the forming soft tissue domain, was sufficient to recapitulate tissue compartmentalization in our model (Figure 5A). Further, we found that domain sizes are insensitive to changes in the magnitude of Wnt, demonstrating that the length scale of the soft tissue compartment is not directly dependent on Wnt diffusion or concentration (Figure 5A). Of note, when we assigned the ectoderm to the exterior of the circular domain, mirroring the right-side-out cross-sectional geometry of the limb bud, our model recapitulates the *in vivo* structural arrangement of dense ECM at the core and densely packed cells at the periphery observed in the limb (Figure 5B). Therefore, a similar process can account for the structural compartmentalization pattern *in vivo*.

To experimentally validate this insensitivity to Wnt diffusive range, we pharmacologically decreased Wnt secretion from the ectoderm[69,73], assaying nuclear β-catenin staining to validate inhibition (Figures 5C-5D). In these conditions, we found that the size of the soft tissue domain, degree of fibronectin clearing, and pattern length scale were maintained

(Figures 5E-5F), matching our *in silico* predictions. Together, these results support a solution to the French Flag problem where the tissue is compartmentalized through structural relations at the cell and supracellular scale (Figure 5G), and the role of an external signal is to spatially bias pattern formation rather than directly encode the length-scale of the pattern through graded control.

Size, separation, and maturity of domains are dependent on inter-level structural relations

While soft tissue and cartilage compartment sizes are not sensitive to levels of Wnt, perturbations in our *in silico* model indicated a sensitivity to levels of cell-supracellular inter-level structural relations. Specifically, reducing or increasing the cell traction and ECM synthesis that would normally occur in response to the forming cell-ECM context (cell-ECM engagement, E) led to an increase in the distance from the ectoderm to the ECM boundary of the cartilage zone in both cases (Figure 6A). To experimentally test these predictions from our *in silico* model, we tuned TRPV4-based Ca^{2+} signaling activity (Figures 2G, S2B, and 3A) and also decreased cell-ECM engagement by inhibiting matrix metalloproteinase (MMP)[74]. In line with our *in silico* results, the distance from the ectoderm to the cartilage increased in all cases (Figures 6B-6C). Specifically, with increased ECM engagement, cartilage cells are overly attracted to each other (note bright fibronectin foci in Figure 6B), and with decreased engagement, cartilage cells do not sufficiently come together (note sparse fibronectin network in Figure 6B). These results support the dependency of pattern length scale on cell-supracellular ECM relations and highlight the predictive strength of our model.

Decreasing cell-ECM engagement also resulted in the loss of a dense, well-aligned supracellular fibronectin network at the edge of the cartilage zone (Figures 6B, 6D, 6E and S5). Coincident with the loss of a clear structural boundary, we observe a loss in sharpness of the separation between Sox9-negative and Sox9-positive cells (Figure 6B), demonstrating that the clear demarcation of compartments, both structurally and for fate, is dependent on the formation of a supracellular fibronectin structure.

Notably, the withdrawal of the Sox9-positive domain when cell-ECM engagement was increased or decreased did not result in a larger compartment of soft tissue fate with increased Twist activation, but rather, Twist expression is diminished in these conditions (Figures 6B-6C and S5B). Further, because both high and low cell-ECM engagement decreased Twist expression, TRPV4 activity does not directly repress Twist expression in a single-cell manner or through driving cartilage fate. Instead, we posited a role for the supracellular structure of the cartilage in the maturation of the soft tissue supracellular structure. Specifically, we hypothesized that such a fibronectin structure in the cartilage is necessary to physically constrain the adjacent soft tissue, promoting an increase in cell density near the ectoderm that further enables cell-cell relations to canalize soft tissue fate (Figure 6F). Indeed, we found that, concomitant to observed decreases in Twist, cell density decreased in the soft tissue domain when we tuned cell-ECM relations both *in silico* and experimentally (Figures 6A-6C and S5B). These results highlight that supracellular structures can interact and condition each other to further canalize fate. Taken together, these results indicate that inter-level cell-ECM relations and the related supracellular structure not only enable cartilage formation but also enable the pattern length scale, a clean boundary, and the conditions for soft domain maturation (Figure 6F).

Conclusion

Viewing a tissue as an ecosystem[25] acknowledges that patterns of cellular differentiation may arise through multi-level causal relationships that are the result of evolutionary processes and

therefore are not simply deducible from physical and chemical laws[12,13,14]. Combining such a perspective with the organite platform led to the identification of key relationships across cellular and supracellular levels of organization that are mechanistically responsible for generating soft tissue and cartilage organization alongside cell differentiation. Articulating the key structural features beyond the cell enabled us to prioritize which chemical and mechanical features are likely to play a role in pattern formation. For instance, our results suggest that precise concentrations or diffusion of Wnt signal are not necessary to robustly specify cell fates or tissue boundaries. It is noteworthy that at subcellular or macromolecular scales, structure is central to investigations of causality and mechanism. Our study illustrates the explanatory capacity of structural biology beyond the cell for the formation of cell fate compartments.

Co-constitution across cell and supracellular levels fuels tissue symmetry-breaking

The inter-scale co-constitution we identify involves not only cells relating in order to generate emergent supracellular structures but also the simultaneous effect of the supracellular structures on cell relations and fate. These findings provide a concrete case study for how an increase in organizational complexity can arise through intrinsic mechanisms that are unique to living systems. Specifically, such co-constitution across levels is not present in bottom-up self-organization characterized in many physical systems[75,76]. Further, while physical models of phase separation, differential adhesion, or molecular reaction diffusion invoke distinct microscopic constituents that then interact to form patterns at larger scales[77,78,79,80,81], the inter-level co-constitution mechanism presented here illustrates how macroscopic differences can arise through an initially homogenous field of constituents. In the mechanism discovered here, symmetry breaking arises on two levels, with cellular agents beginning to differ as they relate, guiding and being guided by a newly forming supracellular structure. While the reciprocal interplay between scales also occurs in the concept of mechanochemical feedback loops[19,20,23], our experimental findings indicate a form of coupling distinct from the current picture of such feedback, because the cellular parts and supracellular structures simultaneously co-create their properties over time[82]. Such inter-level reciprocal constitution is an exciting challenge for future theoretical modeling studies focused on self-organization germane to living systems.

The interlevel co-constitution that we identify here results in a supracellular structure that serves as a top-down cue, canalizing the fate of the cells within. While cell fate changes due to top-down tissue-scale effects from neighboring tissues or microenvironments have been reported in a variety of contexts, including cancer as well as tooth and skin development[45,47,48], here we identify a mechanism in which top-down effects arise from within a tissue itself. Such mechanisms have also been shown to alter cell proliferation and contractility[83,84,85,86]. Importantly, we show that they can be deployed to co-create spatial patterns of structure and cell differentiation. By creating this closed causal loop from within a system[26], limb progenitor mesenchymal tissue is capable of transforming itself into soft tissue and cartilage without the need for an external mechanical or chemical trigger.

Positioning supracellular structure between molecular signaling and cell fate

Our results indicate that the effect of Wnt signal on mesenchymal cell fate is inextricably coupled to supracellular structure. We find that appropriate organization (via cell-cell based linkages) at the supracellular scale is necessary for cells to have the appropriate competency to respond to Wnt signal and activate soft tissue fate in individual cells. The finding that supracellular structure governs the competency of individual cells to respond to signaling molecules opens up an exciting avenue for the study of subcellular-scale molecular dynamics in the context of tissue cell biology[28]. Given that chronic diseases involving inflammation and

fibrosis are rooted in divergent states of tissue organization[87], our results lead us to posit that such disease states may depend on inter-level causation between cell and supracellular level structures. Through this perspective, our work suggests that, in a manner analogous to Wnt, the effects of drugs, carcinogens, or environmental toxins on subcellular processes (e.g. metabolic dysfunction) may be mediated by tissue structural competency.

A new mode of cell fate spatial patterning independent of graded molecular control

The underlying assumption that chemical cues directly instruct individual cells to change cell fate means that cell and supracellular structural considerations are generally missing or subordinated in studies of molecular diffusion-based mechanisms (e.g. reaction-diffusion), especially with regard to causality in pattern initiation[33,69,88,89]. In light of identifying a role for cell and supracellular structural relations in generating patterns and mediating molecular signals, we propose a mechanism of patterning that does not rely on graded molecular control. Such a mechanism may be particularly relevant across mesenchymal and stromal contexts, where the high degree of structural dynamism makes it unlikely that cells are merely static and passive recipients of molecular information[49,90,91,92,93]. Rather than providing information to individual cells in a precise spatial or concentration-dependent manner, we find that Wnt influences the inter-level structural dynamics to bias cells towards soft tissue organization and fate.

While a number of recent studies have incorporated mechanical processes into models of graded molecular control[94,95,96,97], our study suggests that the extent of information provided by Wnt signal regarding spatial pattern is relatively minimal and does not require graded or concentration-based control. Such a mechanism side-steps the issue that molecular gradients as well as transcriptional responses are noisy[98,99,100] because it does not require a highly quantitative or spatially precise transmission of information at the molecular level. Lastly, the notion that the state of cells within a collective could be canalized towards a new state due to the structures that they create and exist within could be a generalizable paradigm in which molecular changes in cells occur in the absence of a clear spatially localized molecular signal.

Acknowledgments: We thank members of the Laboratory of Morphogenesis at The Rockefeller University for discussion and feedback on the manuscript. We thank Drs. Ruslan Medzhitov, Cori Bargmann, and Philip Ball for comments on the manuscript and/or helpful discussions.

Author contributions: A.R.R. and A.E.S. conceived of the project together with C.S.K. A.R.R., A.E.S., and C.S.K directed the conceptual and technical development of the project. A.R.R., A.E.S., C.S.K., and R.C. designed experiments and interpreted results. C.S.K. and R.C. co-developed the organite platform, developed assays, performed experiments, and analyzed results. N.T.M. and K.C. developed assays, performed experiments, and analyzed data, with technical and conceptual guidance from C.S.K., A.R.R., and A.E.S. P.W.M. developed the mathematical model and simulations. A.R.R., A.E.S., and C.S.K. wrote the original draft of the manuscript with input and editing from R.C., N.T.M., and P.W.M. A.E.S and A.R.R co-supervised the project. All authors discussed the results and implications and commented on the manuscript at all stages.

Competing interests: Authors declare that they have no competing interests.

Data and materials availability: All data are available in the main text or the supplementary materials. Code is available here:

https://zenodo.org/records/16784182?preview=1&token=eyJhbGciOiJIUzUxMiJ9.eyJpZCI6IjgwYjcyYzIwLTkzZjctNGIwMy1hYTQwLWIwOGE2YjI1ZDIyYyIsImRhdGEiOnt9LCJyYW5kb20iOiI1MTk1ZDMxMjQ5NDA3NTY3ZjZkZGFlNDg4M2EzZjA0NCJ9.GwtUKBwmBFCd9KjaTGURz52SqhiKU3umqaoHB8EvuuH_RVPkeOnzxyGIEzDcFsLZ1DT45ltNpTzrt4BJ4pOeyQ

Supplementary Materials

Materials and Methods

Supplementary Text

Figs. S1 to S5

Tables S1

Movies S1 to S5

References

1. Schürch CM, Bhate SS, Barlow GL, Phillips DJ, Noti L, Zlobec I, Chu P, Black S, Demeter J, McIlwain DR, Kinoshita S, Samusik N, Goltsev Y, Nolan GP. Coordinated Cellar Neighborhoods Orchestrate Antitumoral Immunity at the Colorectal Cancer Invasive Front. Cell. 2020 Sep 3;182(5):1341-1359.e19. doi: 10.1016/j.cell.2020.07.005. Epub 2020 Aug 6. Erratum in: Cell. 2020 Oct 29;183(3):838. doi: 10.1016/j.cell.2020.10.021. PMID: 32763154; PMCID: PMC7479520.
2. Bressan D, Battistoni G, Hannon GJ. The dawn of spatial omics. Science. 2023 Aug 4;381(6657):eabq4964. doi: 10.1126/science.abq4964. Epub 2023 Aug 4. PMID: 37535749; PMCID: PMC7614974.
3. Liu L, Chen A, Li Y, Mulder J, Heyn H, Xu X. Spatiotemporal omics for biology and medicine. Cell. 2024 Aug 22;187(17):4488-4519. doi: 10.1016/j.cell.2024.07.040. PMID: 39178830.
4. Wolpert L. Positional information and the spatial pattern of cellular differentiation. J Theor Biol. 1969 Oct;25(1):1-47. doi: 10.1016/s0022-5193(69)80016-0. PMID: 4390734.
5. Sharpe J. Wolpert's French Flag: what's the problem? Development. 2019 Dec 20;146(24):dev185967. doi: 10.1242/dev.185967. PMID: 31862794.
6. Ashe HL, Briscoe J. The interpretation of morphogen gradients. Development. 2006 Feb;133(3):385-94. doi: 10.1242/dev.02238. PMID: 16410409.
7. Rogers KW, Schier AF. Morphogen gradients: from generation to interpretation. Annu Rev Cell Dev Biol. 2011;27:377-407. doi: 10.1146/annurev-cellbio-092910-154148. Epub 2011 Jul 29. PMID: 21801015.
8. Green JB, Sharpe J. Positional information and reaction-diffusion: two big ideas in developmental biology combine. Development. 2015 Apr 1;142(7):1203-11. doi: 10.1242/dev.114991. PMID: 25804733.
9. Vargesson N. Positional Information-A concept underpinning our understanding of developmental biology. Dev Dyn. 2020 Mar;249(3):298-312. doi: 10.1002/dvdy.116. Epub 2019 Oct 21. PMID: 31566855.
10. Iber D, Vetter R. Relationship between epithelial organization and morphogen interpretation. Curr Opin Genet Dev. 2022 Aug;75:101916. doi: 10.1016/j.gde.2022.101916. Epub 2022 May 20. PMID: 35605527
11. Kicheva A, Briscoe J. Control of Tissue Development by Morphogens. Annu Rev Cell Dev Biol. 2023 Oct 16;39:91-121. doi: 10.1146/annurev-cellbio-020823-011522. Epub 2023 Jul 7. PMID: 37418774.
12. Rosslenbroich B. Outline of a concept for organismic systems biology. Semin Cancer Biol. 2011 Jun;21(3):156-64. doi: 10.1016/j.semcancer.2011.06.001. Epub 2011 Jun 28. PMID: 21729754.
13. Montévil M, Mossio M, Pocheville A, Longo G. Theoretical principles for biology: Variation. Prog Biophys Mol Biol. 2016 Oct;122(1):36-50. doi: 10.1016/j.pbiomolbio.2016.08.005. Epub 2016 Aug 13. PMID: 27530930.
14. Montévil M. Historicity at the heart of biology. Theory Biosci. 2022 Jun;141(2):165-173. doi: 10.1007/s12064-020-00320-8. Epub 2020 Jul 1. PMID: 32613275.
15. Rosslenbroich B. Properties of Life: Toward a Coherent Understanding of the Organism. Acta Biotheor. 2016 Sep;64(3):277-307. doi: 10.1007/s10441-016-9284-1. Epub 2016 Aug 2. PMID: 27485949.
16. Merle T, Farge E. Trans-scale mechanotransductive cascade of biochemical and biomechanical patterning in embryonic development: the light side of the force. Curr Opin Cell Biol. 2018 Dec;55:111-118. doi: 10.1016/j.ceb.2018.07.003. Epub 2018 Aug 1. PMID: 30077057.
17. Bich L, Pradeu T, Moreau JF. Understanding Multicellularity: The Functional Organization of the Intercellular Space. Front Physiol. 2019 Sep 18;10:1170. doi: 10.3389/fphys.2019.01170. PMID: 31620013; PMCID: PMC6759637.
18. Mongera A, Rowghanian P, Gustafson HJ, Shelton E, Kealhofer DA, Carn EK, Serwane F, Lucio AA, Giammona J, Campàs O. A fluid-to-solid jamming transition underlies vertebrate body axis elongation. Nature. 2018 Sep;561(7723):401-405. doi: 10.1038/s41586-018-0479-2. Epub 2018 Sep 5. PMID: 30185907; PMCID: PMC6148385.
19. Hannezo E, Heisenberg CP. Mechanochemical Feedback Loops in Development and Disease. Cell. 2019 Jun 27;178(1):12-25. doi: 10.1016/j.cell.2019.05.052. PMID: 31251912.
20. Lenne PF, Munro E, Heemskerk I, Warmflash A, Bocanegra-Moreno L, Kishi K, Kicheva A, Long Y, Fruleux A, Boudaoud A, Saunders TE, Caldarelli P, Michaut A, Gros J, Maroudas-Sacks Y, Keren K, Hannezo E, Gartner ZJ, Stormo B, Gladfelter A, Rodrigues A, Shyer A, Minc N, Maître JL, Di Talia S, Khamaisi B, Sprinzak D, Tlili S. Roadmap for the multiscale coupling of biochemical and mechanical signals during development. Phys Biol. 2021 Apr 14;18(4):10.1088/1478-3975/abd0db. doi: 10.1088/1478-3975/abd0db. PMID: 33276350; PMCID: PMC8380410.

21. Petridou NI, Corominas-Murtra B, Heisenberg CP, Hannezo E. Rigidity percolation uncovers a structural basis for embryonic tissue phase transitions. Cell. 2021 Apr 1;184(7):1914-1928.e19. doi: 10.1016/j.cell.2021.02.017. Epub 2021 Mar 16. PMID: 33730596; PMCID: PMC8055543.
22. Huycke TR, Häkkinen TJ, Miyazaki H, Srivastava V, Barruet E, McGinnis CS, Kalantari A, Cornwall-Scoones J, Vaka D, Zhu Q, Jo H, Oria R, Weaver VM, DeGrado WF, Thomson M, Garikipati K, Boffelli D, Klein OD, Gartner ZJ. Patterning and folding of intestinal villi by active mesenchymal dewetting. Cell. 2024 Jun 6;187(12):3072-3089.e20. doi: 10.1016/j.cell.2024.04.039. Epub 2024 May 22. PMID: 38781967; PMCID: PMC11166531.
23. Villeneuve C, Hashmi A, Ylivinkka I, Lawson-Keister E, Miroshnikova YA, Pérez-González C, Myllymäki SM, Bertillot F, Yadav B, Zhang T, Matic Vignjevic D, Mikkola ML, Manning ML, Wickström SA. Mechanical forces across compartments coordinate cell shape and fate transitions to generate tissue architecture. Nat Cell Biol. 2024 Feb;26(2):207-218. doi: 10.1038/s41556-023-01332-4. Epub 2024 Feb 1. PMID: 38302719; PMCID: PMC10866703.
24. Strand DW, Franco OE, Basanta D, Anderson AR, Hayward SW. Perspectives on tissue interactions in development and disease. Curr Mol Med. 2010 Feb;10(1):95-112. doi: 10.2174/156652410791065363. PMID: 20205682; PMCID: PMC4195241.
25. Weiss A, Gralka M, Faust K, Basanta Gutierrez D, Pienta K, Zhou X, Venturelli OS, Gibbons S, Ebrahimkhani MR, Shakiba N, Ma S. How can concepts from ecology enable insights about cellular communities? Cell Syst. 2024 Oct 16;15(10):885-890. doi: 10.1016/j.cels.2024.09.010. Erratum in: Cell Syst. 2024 Nov 20;15(11):1103. doi: 10.1016/j.cels.2024.10.009. PMID: 39418998.
26. Montévil M, Mossio M. Biological organisation as closure of constraints. J Theor Biol. 2015 May 7;372:179-91. doi: 10.1016/j.jtbi.2015.02.029. Epub 2015 Mar 6. PMID: 25752259.
27. Nicholson DJ, Dupré J. Everything Flows: Towards a Processual Philosophy of Biology. Oxford; 2018.
28. Adler M, Chavan AR, Medzhitov R. Tissue Biology: In Search of a New Paradigm. Annu Rev Cell Dev Biol. 2023 Oct 16;39:67-89. doi: 10.1146/annurev-cellbio-120420-113830. Epub 2023 Aug 22. PMID: 37607470.
29. Oster GF, Murray JD, Harris AK. Mechanical aspects of mesenchymal morphogenesis. J Embryol Exp Morphol. 1983 Dec;78:83-125. PMID: 6663234.
30. Oster GF, Shubin N, Murray JD, Alberch P. Evolution and Morphogenetic Rules: The Shape of the Vertebrate Limb in Ontogeny and Phylogeny. Evolution. 1988 Sep;42(5):862-884. doi: 10.1111/j.1558-5646.1988.tb02508.x. PMID: 28581162.
31. Newman SA, Frisch HL. Dynamics of skeletal pattern formation in developing chick limb. Science. **205**, 662-8 (1979). doi: 10.1126/science.462174.
32. Solursh M, Jensen KL, Zanetti NC, Linsenmayer TF, Reiter RS. Extracellular matrix mediates epithelial effects on chondrogenesis in vitro. Dev Biol. 1984 Oct;105(2):451-7. doi: 10.1016/0012-1606(84)90302-6. PMID: 6479446.
33. Sick S, Reinker S, Timmer J, Schlake T. WNT and DKK determine hair follicle spacing through a reaction-diffusion mechanism. Science. 2006 Dec 1;314(5804):1447-50. doi: 10.1126/science.1130088. Epub 2006 Nov 2. PMID: 17082421.
34. Huycke TR, Miller BM, Gill HK, Nerurkar NL, Sprinzak D, Mahadevan L, Tabin CJ. Genetic and Mechanical Regulation of Intestinal Smooth Muscle Development. Cell. 2019 Sep 19;179(1):90-105.e21. doi: 10.1016/j.cell.2019.08.041. PMID: 31539501; PMCID: PMC6756183.
35. Maimets M, Pedersen MT, Guiu J, Dreier J, Thodberg M, Antoku Y, Schweiger PJ, Rib L, Bressan RB, Miao Y, Garcia KC, Sandelin A, Serup P, Jensen KB. Mesenchymal-epithelial crosstalk shapes intestinal regionalisation via Wnt and Shh signalling. Nat Commun. 2022 Feb 7;13(1):715. doi: 10.1038/s41467-022-28369-7. PMID: 35132078; PMCID: PMC8821716.
36. Tavares AT, Izpisúja-Belmonte JC, Rodriguez-León J. Developmental expression of chick twist and its regulation during limb patterning. Int J Dev Biol. 2001 Sep;45(5-6):707-13. PMID: 11669372.
37. Wright E, Hargrave MR, Christiansen J, Cooper L, Kun J, Evans T, Gangadharan U, Greenfield A, Koopman P. The Sry-related gene Sox9 is expressed during chondrogenesis in mouse embryos. Nat Genet. 1995 Jan;9(1):15-20. doi: 10.1038/ng0195-15. PMID: 7704017.
38. Oberlender SA, Tuan RS. Expression and functional involvement of N-cadherin in embryonic limb chondrogenesis. Development. 1994 Jan;120(1):177-87. doi: 10.1242/dev.120.1.177. PMID: 8119125.
39. Kosher RA, Walker KH, Ledger PW. Temporal and spatial distribution of fibronectin during development of the embryonic chick limb bud. Cell Differ. 1982 Jun;11(4):217-28. doi: 10.1016/0045-6039(82)90069-0. PMID: 6749302.

40. Tomasek JJ, Mazurkiewicz JE, Newman SA. Nonuniform distribution of fibronectin during avian limb development. Dev Biol. 1982 Mar;90(1):118-26. doi: 10.1016/0012-1606(82)90217-2. PMID: 7037503.
41. de Almeida PG, Pinheiro GG, Nunes AM, Gonçalves AB, Thorsteinsdóttir S. Fibronectin assembly during early embryo development: A versatile communication system between cells and tissues. Dev Dyn. 2016 Apr;245(4):520-35. doi: 10.1002/dvdy.24391. Epub 2016 Feb 17. PMID: 26845241.
42. Pankov R, Momchilova A, Stefanova N, Yamada KM. Characterization of stitch adhesions: Fibronectin-containing cell-cell contacts formed by fibroblasts. Exp Cell Res. 2019 Nov 1;384(1):111616. doi: 10.1016/j.yexcr.2019.111616. Epub 2019 Sep 6. PMID: 31499058; PMCID: PMC6778521.
43. Sautchuk R Jr, Yang S, Shyer A, Rodrigues A. Epigenetics Beyond the Cell: Supracellular Organization of Fate and Form in Morphogenesis. Cold Spring Harb Perspect Biol. 2025 May 5:a041497. doi: 10.1101/cshperspect.a041497. Epub ahead of print. PMID: 40324838.
44. Shyer AE, Rodrigues AR. Transcending the hegemony of the molecular machine through an organic renewal of biology and biomedicine. Cells Dev. 2025 Mar 10:204018. doi: 10.1016/j.cdev.2025.204018. Epub ahead of print. PMID: 40074200.
45. Nelson CM, Vanduijn MM, Inman JL, Fletcher DA, Bissell MJ. Tissue geometry determines sites of mammary branching morphogenesis in organotypic cultures. Science. 2006 Oct 13;314(5797):298-300. doi: 10.1126/science.1131000. PMID: 17038622; PMCID: PMC2933179.
46. Crest J, Diz-Muñoz A, Chen DY, Fletcher DA, Bilder D. Organ sculpting by patterned extracellular matrix stiffness. Elife. 2017 Jun 27;6:e24958. doi: 10.7554/eLife.24958. PMID: 28653906; PMCID: PMC5503509.
47. Shyer AE, Rodrigues AR, Schroeder GG, Kassianidou E, Kumar S, Harland RM. Emergent cellular self-organization and mechanosensation initiate follicle pattern in the avian skin. Science. 2017 Aug 25;357(6353):811-815. doi: 10.1126/science.aai7868. Epub 2017 Jul 13. PMID: 28705989; PMCID: PMC5605277.
48. Shroff NP, Xu P, Kim S, Shelton ER, Gross BJ, Liu Y, Gomez CO, Ye Q, Drennon TY, Hu JK, Green JBA, Campàs O, Klein OD. Proliferation-driven mechanical compression induces signalling centre formation during mammalian organ development. Nat Cell Biol. 2024 Apr;26(4):519-529. doi: 10.1038/s41556-024-01380-4. Epub 2024 Apr 3. PMID: 38570617; PMCID: PMC11482733.
49. Palmquist KH, Tiemann SF, Ezzeddine FL, Yang S, Pfeifer CR, Erzberger A, Rodrigues AR, Shyer AE. Reciprocal cell-ECM dynamics generate supracellular fluidity underlying spontaneous follicle patterning. Cell. 2022 May 26;185(11):1960-1973.e11. doi: 10.1016/j.cell.2022.04.023. Epub 2022 May 11. PMID: 35551765.
50. Yao M, Tijore A, Cheng D, Li JV, Hariharan A, Martinac B, Tran Van Nhieu G, Cox CD, Sheetz M. Force- and cell state-dependent recruitment of Piezo1 drives focal adhesion dynamics and calcium entry. Sci Adv. 2022 Nov 11;8(45):eabo1461. doi: 10.1126/sciadv.abo1461. Epub 2022 Nov 9. PMID: 36351022; PMCID: PMC9645726.
51. Clapham DE. Calcium signaling. Cell. 2007 Dec 14;131(6):1047-58. doi: 10.1016/j.cell.2007.11.028. PMID: 18083096.
52. Matthews BD, Thodeti CK, Tytell JD, Mammoto A, Overby DR, Ingber DE. Ultra-rapid activation of TRPV4 ion channels by mechanical forces applied to cell surface beta1 integrins. Integr Biol (Camb). 2010 Sep;2(9):435-42. doi: 10.1039/c0ib00034e. Epub 2010 Aug 20. PMID: 20725677; PMCID: PMC3147167.
53. Tytti K, Sanna K, Carla G, Jonatan P, Kaisa R, Sari T. Mechanosensitive TRPV4 channel guides maturation and organization of the bilayered mammary epithelium. Sci Rep. 2024 Mar 21;14(1):6774. doi: 10.1038/s41598-024-57346-x. PMID: 38514727; PMCID: PMC10957991.
54. Muramatsu S, Wakabayashi M, Ohno T, Amano K, Ooishi R, Sugahara T, Shiojiri S, Tashiro K, Suzuki Y, Nishimura R, Kuhara S, Sugano S, Yoneda T, Matsuda A. Functional gene screening system identified TRPV4 as a regulator of chondrogenic differentiation. J Biol Chem. 2007 Nov 2;282(44):32158-67. doi: 10.1074/jbc.M706158200. Epub 2007 Sep 5. PMID: 17804410.
55. Atsuta Y, Tomizawa RR, Levin M, Tabin CJ. L-type voltage-gated Ca^{2+} channel Cav1.2 regulates chondrogenesis during limb development. Proc Natl Acad Sci U S A. 2019 Oct 22;116(43):21592-21601. doi: 10.1073/pnas.1908981116. Epub 2019 Oct 7. PMID: 31591237; PMCID: PMC6815189.
56. Khatib NS, Monsen J, Ahmed S, Huang Y, Hoey DA, Nowlan NC. Mechanoregulatory role of TRPV4 in prenatal skeletal development. Sci Adv. 2023 Jan 25;9(4):eade2155. doi: 10.1126/sciadv.ade2155. Epub 2023 Jan 25. PMID: 36696489; PMCID: PMC9876556.

57. Gardel ML, Schneider IC, Aratyn-Schaus Y, Waterman CM. Mechanical integration of actin and adhesion dynamics in cell migration. Annu Rev Cell Dev Biol. 2010;26:315-33. doi: 10.1146/annurev.cellbio.011209.122036. PMID: 19575647; PMCID: PMC4437624.
58. Ji C, McCulloch CA. TRPV4 integrates matrix mechanosensing with Ca^{2+} signaling to regulate extracellular matrix remodeling. FEBS J. 2021 Oct;288(20):5867-5887. doi: 10.1111/febs.15665. Epub 2020 Dec 23. PMID: 33300268.
59. Woods A, Wang G, Beier F. RhoA/ROCK signaling regulates Sox9 expression and actin organization during chondrogenesis. J Biol Chem. 2005 Mar 25;280(12):11626-34. doi: 10.1074/jbc.M409158200. Epub 2005 Jan 21. PMID: 15665004.
60. Solursh M, Linsenmayer TF, Jensen KL. Chondrogenesis from single limb mesenchyme cells. Dev Biol. 1982 Nov;94(1):259-64. doi: 10.1016/0012-1606(82)90090-2. PMID: 6759202.
61. Benya PD, Shaffer JD. Dedifferentiated chondrocytes reexpress the differentiated collagen phenotype when cultured in agarose gels. Cell. 1982 Aug;30(1):215-24. doi: 10.1016/0092-8674(82)90027-7. PMID: 7127471.
62. ten Berge D, Brugmann SA, Helms JA, Nusse R. Wnt and FGF signals interact to coordinate growth with cell fate specification during limb development. Development. 2008 Oct;135(19):3247-57. doi: 10.1242/dev.023176. PMID: 18776145; PMCID: PMC2756806.
63. Kawakami Y, Capdevila J, Büscher D, Itoh T, Rodríguez Esteban C, Izpisúa Belmonte JC. WNT signals control FGF-dependent limb initiation and AER induction in the chick embryo. Cell. 2001 Mar 23;104(6):891-900. doi: 10.1016/s0092-8674(01)00285-9. PMID: 11290326.
64. Zwiling E. Cartilage formation from so-called myogenic tissue of chick embryo limb buds. Ann Med Exp Biol Fenn. 1966;44:134-139.
65. Kosher RA, Savage MP, Chan SC. In vitro studies on the morphogenesis and differentiation of the mesoderm subjacent to the apical ectodermal ridge of the embryonic chick limb-bud. J Embryol Exp Morphol. 1979 Apr;50:75-97. PMID: 458363.
66. Solursh M, Singley CT, Reiter RS. The influence of epithelia on cartilage and loose connective tissue formation by limb mesenchyme cultures. Dev Biol. 1981 Sep;86(2):471-82. doi: 10.1016/0012-1606(81)90205-0. PMID: 7286409.
67. Daniels K, Reiter R, Solursh M. Micromass cultures of limb and other mesenchyme. Methods Cell Biol. 1996;51:237-47. doi: 10.1016/s0091-679x(08)60631-7. PMID: 8722479.
68. Barna M, Niswander L. Visualization of cartilage formation: insight into cellular properties of skeletal progenitors and chondrodysplasia syndromes. Dev Cell. 2007 Jun;12(6):931-41. doi: 10.1016/j.devcel.2007.04.016. PMID: 17543865.
69. Raspopovic J, Marcon L, Russo L, Sharpe J. Modeling digits. Digit patterning is controlled by a Bmp-Sox9-Wnt Turing network modulated by morphogen gradients. Science. 2014 Aug 1;345(6196):566-70. doi: 10.1126/science.1252960. PMID: 25082703.
70. Miura T, Shiota K. TGFbeta2 acts as an "activator" molecule in reaction-diffusion model and is involved in cell sorting phenomenon in mouse limb micromass culture. Dev Dyn. 2000 Mar;217(3):241-9. doi: 10.1002/(SICI)1097-0177(200003)217:3<241::AID-DVDY2>3.0.CO;2-K. PMID: 10741418.
71. Christley S, Alber MS, Newman SA. Patterns of mesenchymal condensation in a multiscale, discrete stochastic model. PLoS Comput Biol. 2007 Apr 27;3(4):e76. doi: 10.1371/journal.pcbi.0030076. Epub 2007 Mar 8. PMID: 17465675; PMCID: PMC1857812.
72. Cruz MT, Dalgard CL, Ignatius MJ. Functional partitioning of beta1 integrins revealed by activating and inhibitory mAbs. J Cell Sci. 1997 Nov;110 (Pt 21):2647-59. doi: 10.1242/jcs.110.21.2647. PMID: 9427383.
73. Chen B, Dodge ME, Tang W, Lu J, Ma Z, Fan CW, Wei S, Hao W, Kilgore J, Williams NS, Roth MG, Amatruda JF, Chen C, Lum L. Small molecule-mediated disruption of Wnt-dependent signaling in tissue regeneration and cancer. Nat Chem Biol. 2009 Feb;5(2):100-7. doi: 10.1038/nchembio.137. Epub 2009 Jan 4. PMID: 19125156; PMCID: PMC2628455.
74. Lu P, Takai K, Weaver VM, Werb Z. Extracellular matrix degradation and remodeling in development and disease. Cold Spring Harb Perspect Biol. 2011 Dec 1;3(12):a005058. doi: 10.1101/cshperspect.a005058. PMID: 21917992; PMCID: PMC3225943.
75. Haken H. Information and self-organization. A macroscopic approach to complex systems. Springer Berlin Heidelberg; 2006. Available from: https://link.springer.com/book/10.1007/3-540-33023-2.
76. Yates FE. Self-organizing systems. The emergence of order. Plenum press; 1987. Available from: https://link.springer.com/book/10.1007/978-1-4613-0883-6.

77. Turing AM. The chemical basis of morphogenesis. Phil. Trans. R. Soc. Lond. 1952 Aug 14;37-72. doi:10.1098/rstb.1952.0012.
78. Foty RA, Steinberg MS. The differential adhesion hypothesis: a direct evaluation. Dev Biol. 2005 Feb 1;278(1):255-63. doi: 10.1016/j.ydbio.2004.11.012. PMID: 15649477.
79. Gonzalez-Rodriguez D, Guevorkian K, Douezan S, Brochard-Wyart F. Soft matter models of developing tissues and tumors. Science. 2012 Nov 16;338(6109):910-7. doi: 10.1126/science.1226418. PMID: 23161991.
80. Wang B, Zhang L, Dai T, Qin Z, Lu H, Zhang L, Zhou F. Liquid-liquid phase separation in human health and diseases. Signal Transduct Target Ther. 2021 Aug 2;6(1):290. doi: 10.1038/s41392-021-00678-1. PMID: 34334791; PMCID: PMC8326283
81. Wang S, Garcia-Ojalvo J, Elowitz MB. Periodic spatial patterning with a single morphogen. Cell Syst. 2022 Dec 21;13(12):1033-1047.e7. doi: 10.1016/j.cels.2022.11.001. Epub 2022 Nov 25. PMID: 36435178.
82. Pfeifer CR, Shyer AE, Rodrigues AR. Creative processes during vertebrate organ morphogenesis: Biophysical self-organization at the supracellular scale. Curr Opin Cell Biol. 2024 Feb;86:102305. doi: 10.1016/j.ceb.2023.102305. Epub 2024 Jan 4. PMID: 38181658.
83. Nelson CM, Jean RP, Tan JL, Liu WF, Sniadecki NJ, Spector AA, Chen CS. Emergent patterns of growth controlled by multicellular form and mechanics. Proc Natl Acad Sci U S A. 2005 Aug 16;102(33):11594-9. doi: 10.1073/pnas.0502575102. Epub 2005 Jul 27. PMID: 16049098; PMCID: PMC1187971.
84. Lander AD. Pattern, growth, and control. Cell. 2011 Mar 18;144(6):955-69. doi: 10.1016/j.cell.2011.03.009. PMID: 21414486; PMCID: PMC3128888.
85. Bosveld F, Markova O, Guirao B, Martin C, Wang Z, Pierre A, Balakireva M, Gaugue I, Ainslie A, Christophorou N, Lubensky DK, Minc N, Bellaïche Y. Epithelial tricellular junctions act as interphase cell shape sensors to orient mitosis. Nature. 2016 Feb 25;530(7591):495-8. doi: 10.1038/nature16970. Epub 2016 Feb 17. Erratum in: Nature. 2016 Mar 16;534(7605):138. doi: 10.1038/nature17622. PMID: 26886796; PMCID: PMC5450930.
86. Chanet S, Miller CJ, Vaishnav ED, Ermentrout B, Davidson LA, Martin AC. Actomyosin meshwork mechanosensing enables tissue shape to orient cell force. Nat Commun. 2017 May 15;8:15014. doi: 10.1038/ncomms15014. PMID: 28504247; PMCID: PMC5440693.
87. Soto AM, Sonnenschein C. The tissue organization field theory of cancer: a testable replacement for the somatic mutation theory. Bioessays. 2011 May;33(5):332-40. doi: 10.1002/bies.201100025. PMID: 21503935; PMCID: PMC3933226.
88. Balaskas N, Ribeiro A, Panovska J, Dessaud E, Sasai N, Page KM, Briscoe J, Ribes V. Gene regulatory logic for reading the Sonic Hedgehog signaling gradient in the vertebrate neural tube. Cell. 2012 Jan 20;148(1-2):273-84. doi: 10.1016/j.cell.2011.10.047. PMID: 22265416; PMCID: PMC3267043.
89. Ramos R, Swedlund B, Ganesan AK, Morsut L, Maini PK, Monuki ES, Lander AD, Chuong CM, Plikus MV. Parsing patterns: Emerging roles of tissue self-organization in health and disease. Cell. 2024 Jun 20;187(13):3165-3186. doi: 10.1016/j.cell.2024.05.016. PMID: 38906093; PMCID: PMC11299420.
90. Ettinger L, Doljanski F. On the generation of form by the continuous interactions between cells and their extracellular matrix. Biol Rev Camb Philos Soc. 1992 Nov;67(4):459-89. doi: 10.1111/j.1469-185x.1992.tb01190.x. PMID: 1463809.
91. Maffini MV, Soto AM, Calabro JM, Ucci AA, Sonnenschein C. The stroma as a crucial target in rat mammary gland carcinogenesis. J Cell Sci. 2004 Mar 15;117(Pt 8):1495-502. doi: 10.1242/jcs.01000. Epub 2004 Mar 2. PMID: 14996910.
92. Pakshir P, Alizadehgiashi M, Wong B, Coelho NM, Chen X, Gong Z, Shenoy VB, McCulloch CA, Hinz B. Dynamic fibroblast contractions attract remote macrophages in fibrillar collagen matrix. Nat Commun. 2019 Apr 23;10(1):1850. doi: 10.1038/s41467-019-09709-6. Erratum in: Nat Commun. 2019 May 20;10(1):2286. doi: 10.1038/s41467-019-10344-4. PMID: 31015429; PMCID: PMC6478854.
93. Plikus MV, Wang X, Sinha S, Forte E, Thompson SM, Herzog EL, Driskell RR, Rosenthal N, Biernaskie J, Horsley V. Fibroblasts: Origins, definitions, and functions in health and disease. Cell. 2021 Jul 22;184(15):3852-3872. doi: 10.1016/j.cell.2021.06.024. PMID: 34297930; PMCID: PMC8566693.
94. Xiong F, Tentner AR, Huang P, Gelas A, Mosaliganti KR, Souhait L, Rannou N, Swinburne IA, Obholzer ND, Cowgill PD, Schier AF, Megason SG. Specified neural progenitors sort to form sharp domains after noisy Shh signaling. Cell. 2013 Apr 25;153(3):550-61. doi: 10.1016/j.cell.2013.03.023. PMID: 23622240; PMCID: PMC3674856.

95. Parada C, Banavar SP, Khalilian P, Rigaud S, Michaut A, Liu Y, Joshy DM, Campàs O, Gros J. Mechanical feedback defines organizing centers to drive digit emergence. Dev Cell. 2022 Apr 11;57(7):854-866.e6. doi: 10.1016/j.devcel.2022.03.004. PMID: 35413235.
96. Pinheiro D, Kardos R, Hannezo É, Heisenberg CP. Morphogen gradient orchestrates pattern-preserving tissue morphogenesis via motility-driven unjamming. Nat. Phys. 2022 Oct 24;18:1482–1493. doi: 10.1038/s41567-022-01787-6.
97. Clarke DN, Miller PW, Martin AC. EGFR-dependent actomyosin patterning coordinates morphogenetic movements between tissues in Drosophila melanogaster. Dev Cell. 2025 Jan 20;60(2):270-287.e6. doi: 10.1016/j.devcel.2024.10.002. Epub 2024 Oct 25. PMID: 39461341; PMCID: PMC11755374.
98. Stathopoulos A, Iber D. Studies of morphogens: keep calm and carry on. Development. 2013 Oct;140(20):4119-24. doi: 10.1242/dev.095141. PMID: 24086076; PMCID: PMC3787753.
99. Akieda Y, Ogamino S, Furuie H, Ishitani S, Akiyoshi R, Nogami J, Masuda T, Shimizu N, Ohkawa Y, Ishitani T. Cell competition corrects noisy Wnt morphogen gradients to achieve robust patterning in the zebrafish embryo. Nat Commun. 2019 Oct 17;10(1):4710. doi: 10.1038/s41467-019-12609-4. PMID: 31624259; PMCID: PMC6797755.
100. Aoki K, Higuchi T, Akieda Y, Matsubara K, Ohkawa Y, Ishitani T. Mechano-gradients drive morphogen-noise correction to ensure robust patterning. Sci Adv. 2024 Nov 15;10(46):eadp2357. doi: 10.1126/sciadv.adp2357. Epub 2024 Nov 15. PMID: 39546611; PMCID: PMC11567007.

Figure 1

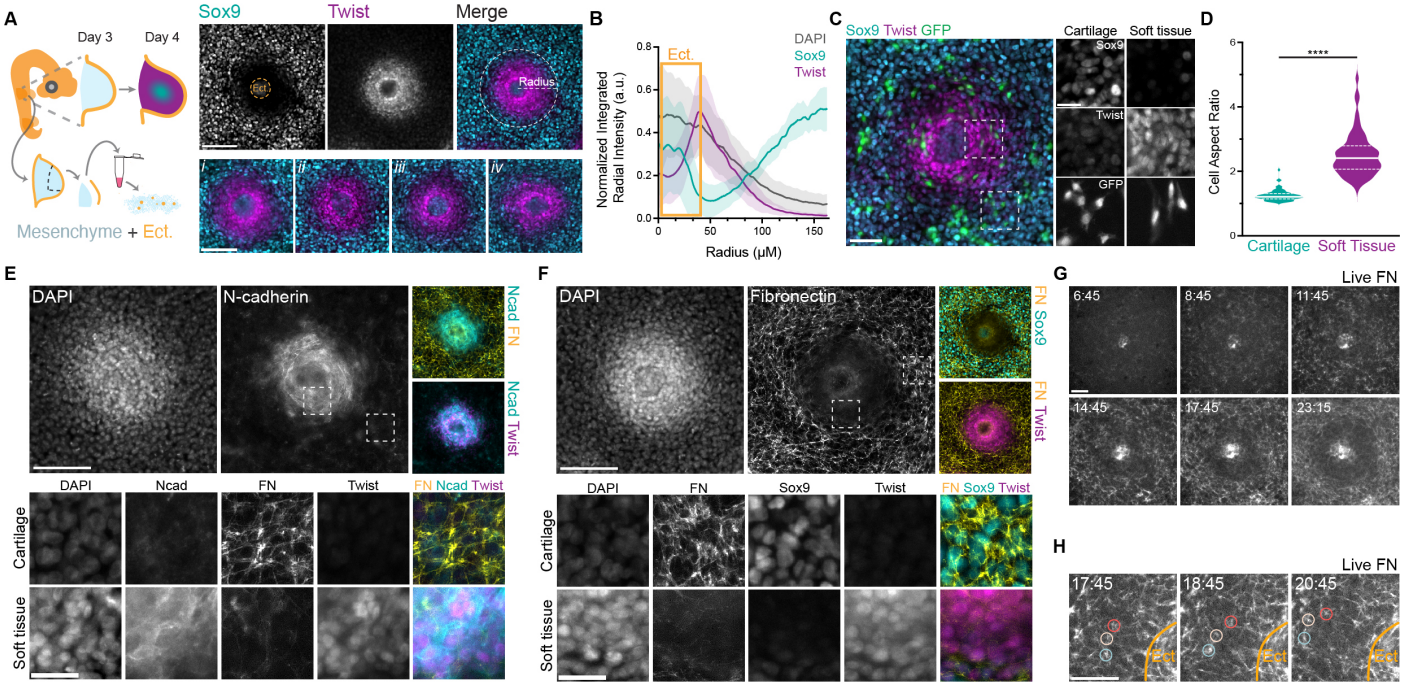

Figure 1. The organite platform reconstitutes the formation of distinct domains of cell fate and supracellular organization corresponding to cartilage and soft tissues. (A) Left, schematic of organite platform, which results in epithelial tissue embedded in a field of cartilage. Right, maximum intensity projections of nuclei (DAPI), Sox9, and Twist in an organite. Sox9 is expressed in the ectoderm (see also fig. S1A). Additional replicates are shown below. Scale bars, 100 μm **(B)** Radial intensity profiles of normalized mean integrated intensities of DAPI (grey), Sox9 (green), and Twist (purple) measured from the center of the ectodermal tissue (orange dashed circle in 1A). **(C)** Sox9 and Twist in an organite with <5% GFP cells reveal soft tissue cells are more elongated than cartilage cells. Scale bars, 50 μm (left) and 20 μm (right). **(D)** Quantification of cell aspect ratios comparing cartilage and soft tissue. Violin plots show median and quartiles. **** $p < .0001$. (E) Top, DAPI, Ncad, fibronectin (FN), and Twist staining in an organite show high levels of Ncad in soft tissue. Scale bar, 100 μm. Crops of regions highlighted by dashed boxes shown below. Scale bar, 25 μm. **(F)** Top, DAPI, FN, Sox9, and Twist staining in an organite show FN is present at lower overall density in the soft tissue, whereas the cartilage tissue forms a dense network. Scale bar, 100 μm. Crops of regions highlighted by dashed boxes shown below. Scale bar, 25 μm. (**G**) Montage from a live imaging experiment visualizing fibronectin in organites (Movie S1). Scale bar, 50 μm. (**H**) Montage where FN foci are marked with colored circles and tracked over time, showing displacement away from the ectoderm (Movie S2). Scale bar, 50 μm.

Figure 2

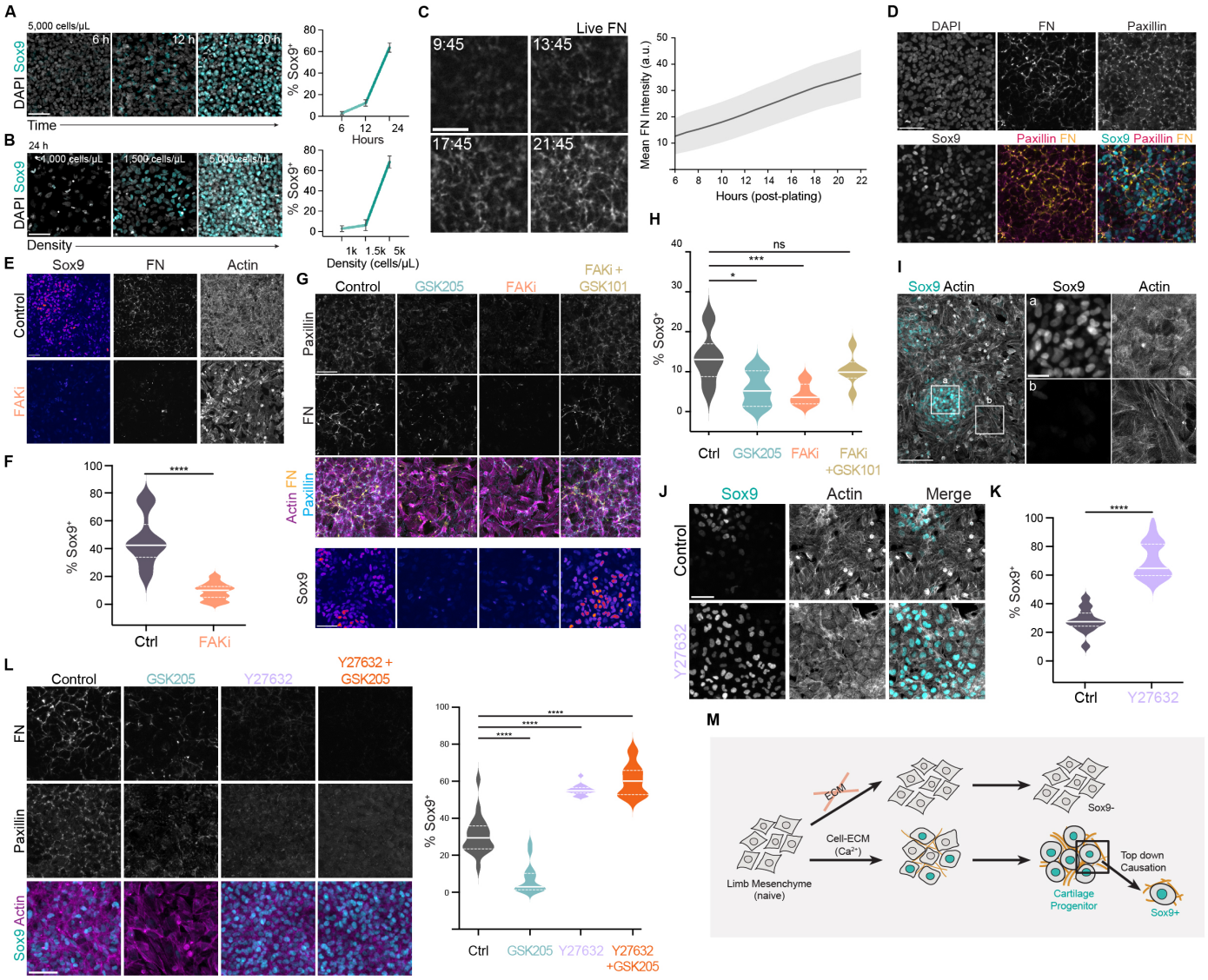

Figure 2. Cell-ECM interactions enable a supracellular-level impulse for cartilage fate activation. (A) Left, Sox9 levels increase over time until most limb progenitor cells adopt cartilage fate by 24 hours of culture. Right, Quantification of %Sox9+ area. **(B)** Left, DAPI and Sox9 in 24-hour *ex vivo* cultures plated at different densities show Sox9 activation is density dependent. Right, Quantification of %Sox9+ area. **(C)** Left, montage from live imaging of fibronectin in *ex vivo* cultures (Movie S3). Right, mean fibronectin intensity over time. **(D)** Focal adhesion components are enriched at interfaces between cells in 24-hour *ex vivo* cultures. **(E)** *Ex vivo* cultures treated with 10 μM FAKi display reduced Sox9 and FN and cell-cell associations. **(F)** Quantification of %Sox9+ area. *** $p < .0001$. **(G)** Sox9, Paxillin, FN, and Actin in 24-hour *ex vivo* cultures treated with FAKi, GSK205 (TRPV4 antagonist 50 μM), and GSK101 (TRPV4 agonist 15 μM). Sox9 images are from a separate replicate. **(H)** Quantification of %Sox9+ area. *** $p = 0.0004$; * $p = 0.0110$; ns, not significant. **(I)** *Ex vivo* limb progenitor cell culture stained for actin and Sox9. Scale bars, 100 μm (left) and 50 μm (right). **(J)** Sox9 and actin in *ex vivo* cultures treated with 10 μM Y27632. **(K)** Quantification of % Sox9+ area. **** $p < .0001$. **(L)** FN, Paxillin, Sox9, and Actin in *ex vivo* cultures treated with GSK205 (50 μM) and Y27632 (ROCK inhibitor, 10 μM). Right, quantification of % Sox9+ area. **** $p < .0001$. **(M)** Schematic showing cell-ECM structural formation guides cytoskeletal architecture toward the confirmation necessary for Sox9 activation. All violin plots show median and interquartile range; all scale bars = 50 μm; all error bars represent mean ± SD unless otherwise noted.

Figure 3

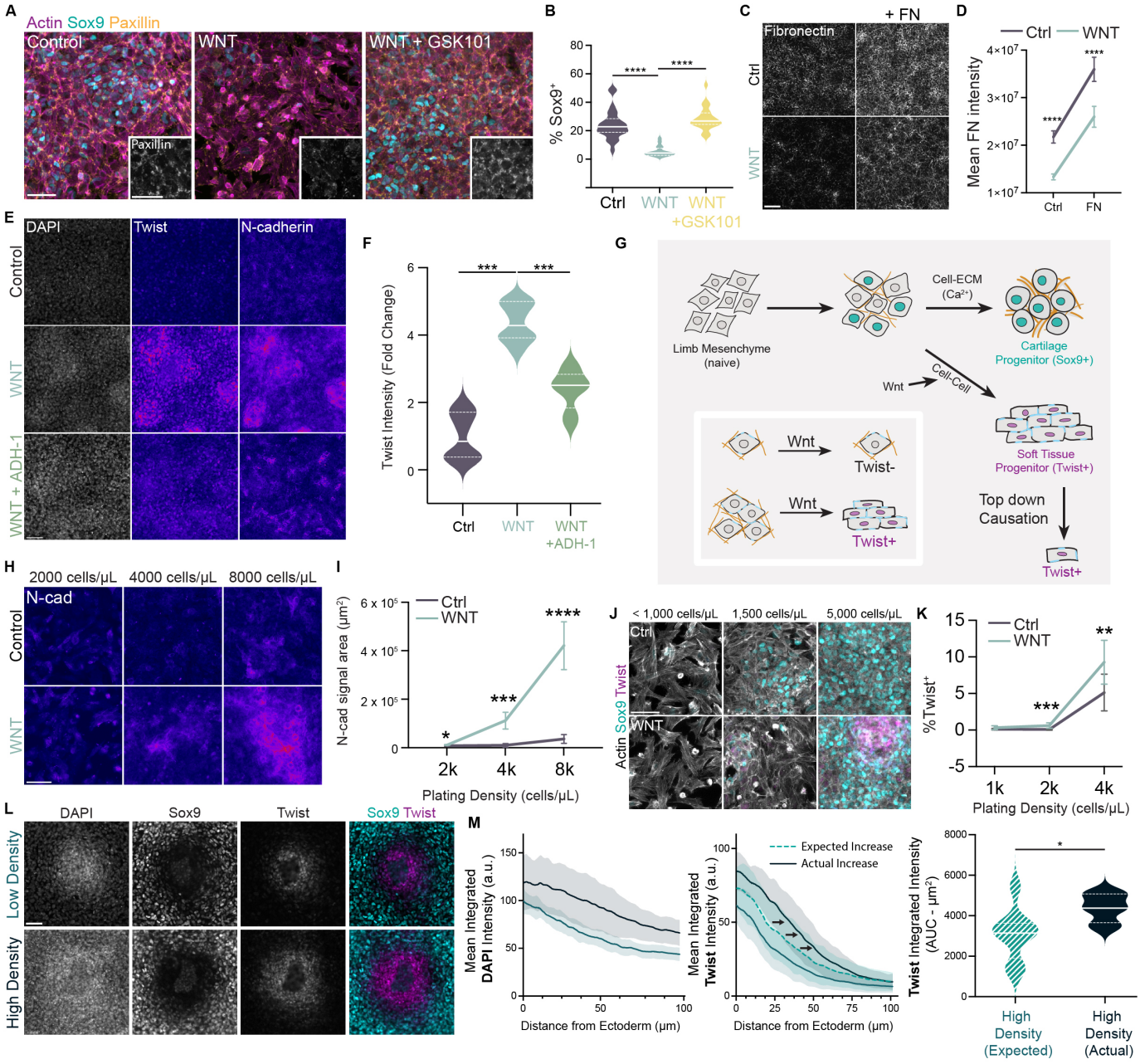

Figure 3. Wnt activation of soft tissue fate is mediated by cell-cell interactions. (A) Treatment with 15 μM GSK101 rescues cell-ECM engagement and cellular cohesion in Wnt-treated cultures to restore Sox9. **(B)** %Sox9+ area of 3A. **** $p < .0001$. **(C)** Fibronectin staining of control and Wnt-treated *ex vivo* cultures supplemented with exogenous FN (5 μg/mL). Scale bar, 100 μm. **(D)** Mean FN intensity comparison of 3C. **** $p < .0001$. **(E)** High density (10,000 cells/μL) *ex vivo* cultures treated with Wnt alone or in addition to .25 mg/mL of the Ncad inhibitor ADH-1 stained for DAPI, Ncad, and Twist show Wnt induces aggregation and Twist activation through Ncad. **(F)** Quantification of fold change in Twist intensity normalized to DAPI. *** $p = .0002$. **(G)** Wnt guides cells toward soft tissue fate by promoting a supracellular structure stemming from Ncad-based cell-cell adhesion. **(H)** Ncad in control or Wnt-treated *ex vivo* cultures of different densities shows Wnt induces Ncad activation at the collective cell scale. **(I)** Quantification of Ncad+ area. **** $p < .0001$; *** $p = 0.0002$; ** $p = .0162$. **(J)** Wnt treatment (150 ng/mL) in *ex vivo* cultures at different plating densities shows induction of soft tissue fate (Twist) downstream of Wnt is density dependent. **(K)** Quantification of %Twist+ area of 3J *** $p < .0001$; ** $p = .0003$. **(L)** Organites with low (5,000 cells/μL) or high cell density (20-40,000 cells/μL). **(M)** Radial intensity profile of normalized mean integrated intensities of DAPI (left) and Twist (middle) in low- and high-density organites. Dashed line represents expected Twist signal based on DAPI intensity. Right, Area under the curve (AUC) comparison of expected and actual total integrated Twist intensities in high-density cultures. * $p = .0371$. All violin plots show median and interquartile range; all scale bars = 50 μm; all error bars represent mean ± SD unless otherwise noted.

Figure 4

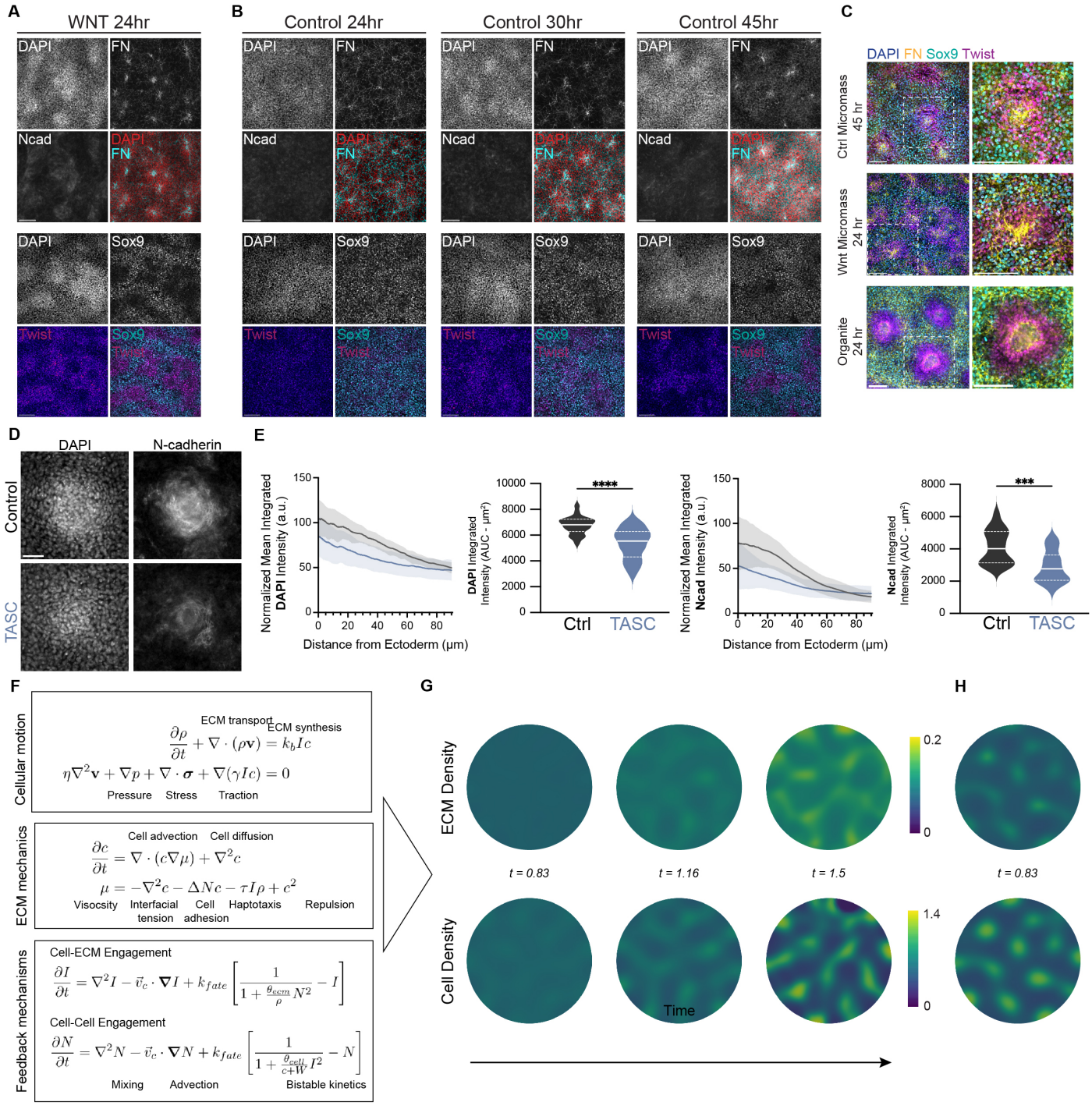

Figure 4. Cartilage and soft tissue domains can arise in the absence of a spatially localized epithelial signal. (A) Top, DAPI, FN, and Ncad in 24-hour, 30-hr, and 45-hr culture limb micromasses (from left to right). Bottom, DAPI, Sox9, and Twist. **(B)** DAPI, FN, and Ncad in a Wnt-treated 24-hour limb micromass (top) and DAPI, Sox9, and Twist (bottom) in a Wnt-treated 24-hour limb micromass. **(C)** Merged images of DAPI, fibronectin, Sox9, and Twist in a 45-hour control micromass (top) and a 24-hour micromass treated with Wnt (middle) show similarities in organization to organite culture (bottom). **(D)** DAPI and Ncad in control and TASC-treated (20 µg/mL) organites. **(E)** Radial intensity profiles and AUC analysis of normalized mean integrated intensities of DAPI and Ncad from (A) measured as distance from the ectoderm, TASC in blue. Mean ± SD shown. Violin plots show median and interquartile range. **** $p < .0001$; *** $p = 0.0005$ **(F)** Key equations of mathematical model describing ECM transport and mechanics (top), cellular transport (middle), and feedback from the supracellular environment (bottom). See Supplemental Material for full details. **(G)** Cell and ECM densities in control micromass simulation, $S_w = 0$, at three time points T=.83, 1.16, and 1.5 (dimensionless units). **(H)** Cell and ECM densities in micromasses simulations with high Wnt dosage ($S_W = 4$) at time point T=0.83 exhibit accelerated pattern formation compared to the control micromass at the same time point. Scale bar = 100 µm unless noted otherwise.

Figure 5

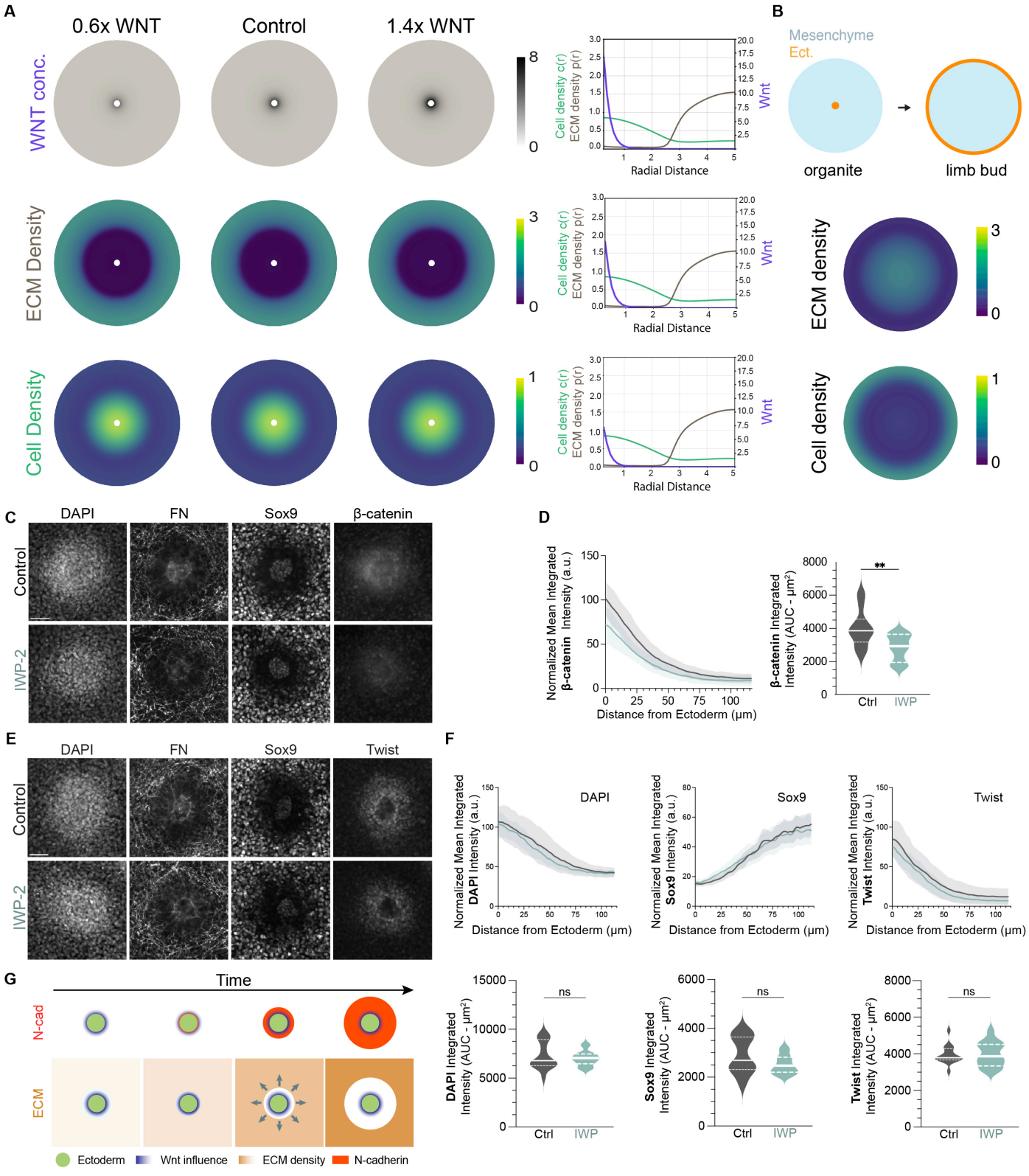

Figure 5. Spatiotemporal specification of domain pattern through a bistability in cellular relations promoted by Wnt bias. (A) Simulations of the organite system with ectodermal Wnt factor set at $S_{ect} = 3$ (low), 5 (control), and 7 (high) show negligible differences in ECM and cell density distributions, indicating that patterning length scales are set by bulk dynamics rather than through ectodermal signal strength. **(B)** Simulation of cell and ECM densities on a disk domain of radius $R = 5$ where Wnt is introduced from the boundary (see diagram on left) reproduces *in vivo* tissue organization. **(C)** Decreased nuclear β-catenin in 5 μM IWP-2-treated organites as compared to control confirms reduction in Wnt signal. **(D)** Left, radial intensity profile of normalized mean integrated intensities of β-catenin measured from the ectoderm. Right, AUC analysis comparing total integrated intensities of β-catenin plots between control and IWP-treated organites. ** p = .0063. **(E)** DAPI, FN, Sox9, and Twist staining in control and 5 μM IWP-2-treated organites show that reducing Wnt secretion (IWP-2) has negligible effects on organite patterning. **(F)** Top, radial intensity profiles of normalized mean integrated intensities. Bottom, AUC analyses comparing the total integrated intensities of above plots between control and IWP-treated organites. ns, not significant. **(G)** Schematic showing that pattern length scale is established through a supracellular instability, whereby increases in cell-cell interactions near the ectoderm cause fibronectin clearing towards the emerging cartilage, where cell-ECM interactions dominate. All violin plots show median and interquartile range; all scale bars = 50 μm; all error bars represent mean ± SD unless otherwise noted.

Figure 6

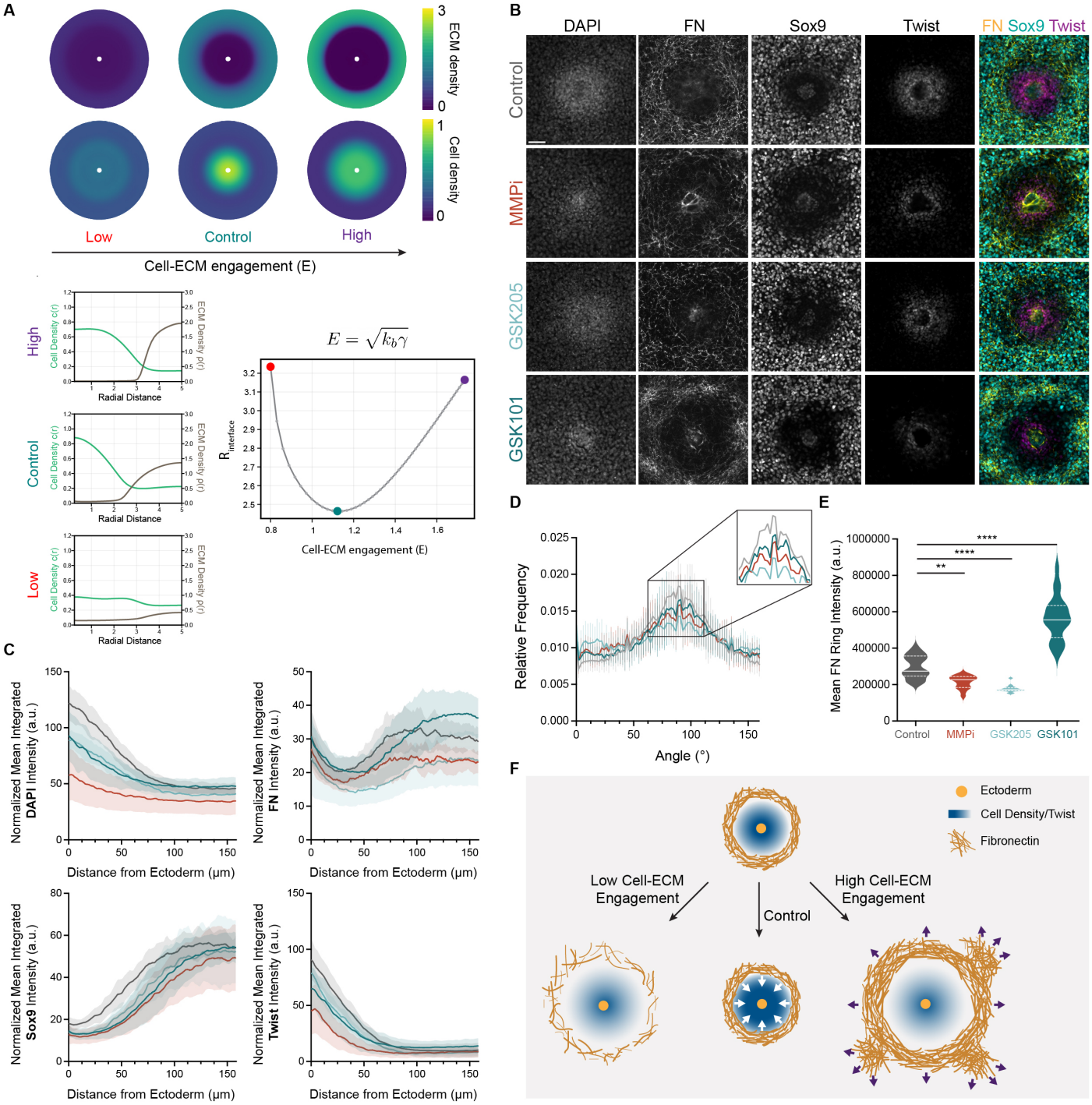

Figure 6. Inter-level structural relations establish the pattern length scale, boundary, and mutual conditioning of domains. (A) Top, Simulation snapshots at $T = 4$ subject to changing cell-ECM interactions showing increased ECM clearance and reduced cell density near the ectoderm when cell-ECM engagement is increased ($\gamma: 0.77 \rightarrow 1.1, k_b: 2.8 \rightarrow 3.1$) or decreased ($\gamma: 0.77 \rightarrow 0.4, k_b: 2.8 \rightarrow 1.6$). Right, effective radius of ECM ring ($\boldsymbol{R_{eff} = \int r|\nabla I|^2\, dx\, /\, \int |\nabla I|^2\, dx}$) plotted against cell-ECM engagement $\boldsymbol{E = \sqrt{\gamma k_b}}$. **(B)** Organites treated with 30 μM MMPi (Batimastat), GSK205 (TRPV4 antagonist, 50 μM), and GSK101 (TRPV4 agonist, 15 μM) show disrupted ECM network formation, change in pattern length scale, and reduced Twist activation. Scale bar, 50 μm. **(C)** Mean radial intensity profiles of normalized integrated intensities measured from the ectoderm. Mean ± SD shown. **(D)** Histogram of fibronectin fiber orientation angles within the FN ring immediately neighboring the soft tissue (also fig. 5A). A χ^2 test was performed comparing each treatment group to control: MMPi, p = .0203; GSK205, p <.0001; GSK101, ns. **(E)** Comparison of mean integrated intensity of FN measured in 5D. Violin plots show median and quartiles. ** p = .0039; **** p < .0001. **(F)** Schematic depicting that fibronectin structure in the cartilage is necessary to physically limit the adjacent soft tissue, promoting the increase in cell density needed for Twist activation.

Supplemental Information

Title: **Cell-supracellular structural relations solve the French Flag Problem without graded molecular control**

Authors: Clint S. Ko[1,3], Ruonan Chen[1,3], Nina T. Magid[1], Pearson W. Miller[2]*, Alan R. Rodrigues[1,4]*, Amy E. Shyer[1,4]*

Included in this PDF file:

Materials and Methods
Supplemental Material
Figs. S1 to S5
Legends for Movies S1 to S5
Table S1

Additional Supplementary Materials include:

Movies S1 to S5

Materials and Methods

Embryos and dissections

Fertilized chicken eggs (white leghorn) were obtained from commercial sources, incubated at 37.8°C , and staged according to Hamburger and Hamilton. GFP-labeled embryos used in this study were obtained from Clemson University and maintained in a manner similar to wild-type embryos. Primary cells were obtained from embryonic day 4 forelimbs (HH21), collecting only up to the distal third of the bud and removing the posterior region to remove influences from the zone of polarizing activity. Buds were dissected in PBS and transferred to a plate where they sat in a mixture of trypsin and collagenase at room temperature for 10 min. Limb mesenchyme was manually separated from ectoderms in full media (10% fetal bovine serum, 1% penicillin-streptomycin and 2% chick serum in DMEM).

Cell culture assays

Ex vivo cultures and micromasses

Mesenchymal tissue from dissected buds (prepared as described above) were collected and mechanically dissociated with a micropipette. The suspension was passed through a 40 µm cell strainer (Corning) and spun down in a centrifuge at 200 rcf for 5 minutes. Supernatant was removed, and cells were resuspended in full media in the appropriate volume to produce low- or high-density suspensions. Cell suspensions were plated as 10 µL drops on standard 24-well plates for *ex vivo* assays or Ibidi 15-well µ slides for micromasses (Cat. #81506) and incubated at 39°C for 2 hours before full media (with or without treatments) were added. For cultures that went longer than 24 hrs (micromasses at 30 and 45 hrs in Figure 6), media was replaced daily. For Fig. S2B-C, Matrigel (Corning) was added to the cell suspension in full media until the final concentration was 3 mg/mL. These suspensions were plated and left at room temperature for 5 minutes to let the Matrigel solidify slightly before the plates were transferred to an incubator.

Organite platform

Organites were prepared in a similar fashion to our *ex vivo* or micromass cultures, except for these assays ectodermal tissue was included with the mesenchymal tissue before mechanical dissociation. Thus, rather than peeling away all ectoderms after collagenase/trypsin treatment during embryo dissections, a percentage of excised limb forelimbs were left unpeeled (60-80%). Cell suspensions of mesenchymal and epithelial tissue were plated in 10 µL drops in Ibidi 8-well chamber slides for organites (Cat. #80826). For Fig. 1C, limb buds from GFP-labeled embryos were mixed in, typically at <5% of all limb buds.

Treatments

The following pharmacological agents were utilized across cell culture assays: FAKi (FAK inhibitor 14, Tocris, Cat. 3414; 10 µM), Y-27632 (Tocris, Cat. 1254; 10 µM, TRPV4 inhibitor (GSK205, MedChemExpress, HY-120691A; 50 µM), TRPV4 activator (GSK101, Selleck, Cat. S8107; 15 µM), Wnt inhibitor (IWP-2, Tocris, Cat. 3533; 5 µM), MMP inhibitor (Batimastat, Tocris, Cat. 2961; 30 µM), Calmodulin inhibitor (Fig. S2C) (W-7, Tocris, Cat. 0369; 1 µM). In addition, we utilized the following proteins and peptides as treatments across all our assays: Wnt (Human Wnt-3a, Tocris, Cat. 5036-WN; 75 – 150 ng/mL), Fibronectin (Recombinant human fibronectin protein, Tocris, Cat. 4305-FNB; 5 µg/mL), N-cad inhibitor (ADH-1, MedChemExpress, HY-13541; .25 mg/mL), Integrin activating antibody (TASC, Sigma-Aldrich, MAB19294; 20 µg/mL). To produce ectoderm-conditioned media used in Fig. S4A, 39-44 peeled ectoderms were collected and cultured in 50 µL of full media for 3-4 days. (A larger or smaller volume of conditioned media was prepared keeping the ratio of 40 ectoderms/50uL full media.) After culture, the media was collected and filtered through a 20um

filter (Pluriselect, 43-10020-40) before being added to plated mesenchymal cells. Due to the low volumes collected, we used Ibidi 15-well µ slides (Cat. #81506) so that we could add 10-20 µL of conditioned media to limb cultures.

Immunofluorescence and Imaging

In vitro culture assays

All *ex vivo*/*in vitro* samples were fixed in 4% paraformaldehyde in PBS for 20 minutes at room temperature. After washes in PBS and PBTx (0.1% Triton-X in PBS), samples were treated with CAS-Block (Invitrogen) for 30 minutes at room temperature. Once the blocking agent was removed, samples were incubated with primary antibodies diluted in 10% CAS in PBTx for 2-3 hours at room temperature or overnight at 4°C. The following primary antibodies and dilutions were used: Sox9 (Abcam, ab5535; 1:1000), Twist (Santa Cruz, sc-81417; 1:300), N-cadherin (Proteintech, 22018-1-AP; 1:300), AF488-conjugated Fibronectin (Thermo Fisher, 53-9869-80; 1:300), Paxillin (5H11) (Thermo Fisher, AHO0492; 1:300), β-catenin (12F7) (Santa Cruz, sc-59737; 1:100), β1 Integrin (Sigma Aldrich, I8638, 1:300), Vinculin (Sigma Aldrich, V9131, 1:300).

After staining with primary antibodies, samples were washed with PBTx and then incubated with secondary antibodies diluted in 10% CAS in PBTx for 2-3 hours at room temperature or overnight at 4°C. The following secondary antibodies and dilutions were used: DAPI (Invitrogen, D1306, 1:1000), Alexa Fluor 488 (Invitrogen, 1:300), Alexa Fluor 555 (Invitrogen, 1:300), Alexa Fluor 647 (Invitrogen, 1:300), ReadyProbes Phalloidin conjugates (Thermo Fisher, Cat. R37112, 1 drop/mL). After staining, samples were imaged on a Nikon ECLIPSE Ti2 with either a Plan Apo 4X (NA 0.2) or S Plan Fluor 20X (NA 0.45) objective. Some images (Fig. 4C, right side of panels from 6A-B; E) were imaged on a Zeiss LSM980 with a 25X objective.

In vivo sections

For visualization of limb tissue (Fig. S1 and S2D), whole embryos were fixed in 4% paraformaldehyde overnight at 4°C and then transferred to 20% sucrose in PBS for another overnight incubation. Limb buds were cut within the sucrose solution with forceps and transferred to Tissue-Tek O.C.T. compound (Sakura) and stored at -80°C. These frozen samples were sectioned with a Cryostat (Leica CM3050S) and tissue sections were collected on Superfrost slides (Fisherbrand). Slides were treated with the same immunostaining protocol described above.

Live imaging

Both standard *ex vivo* culture assays and organites were plated in Ibidi 8-well chamber slides (Cat. #80826), and imaged in a Zeiss Celldiscoverer 7. The culture chamber was set at 37°C and images were acquired once every 6 minutes with a 20X objective lens set to 0.5x zoom. For live visualization of fibronectin in *ex vivo* assays or organites, AF488-conjugated FN antibody was added to the media (1:300 dilution).

Image Analysis and quantification

Prior to analysis, all images were processed by first producing a maximum intensity projection with all z slices that were in focus (typically 2 – 4 slices). Some images were additionally processed with background subtraction (see below).

Analysis of DAPI, Sox9, Twist, and FN profiles in the organite platform was performed using the Radial Profile Angle FIJI plugin (https://imagej.net/ij/plugins/radial-profile.html). The radius was set at 600 pixels (Fig. 5), 500 pixels (Fig. 1B), 450 pixels (Fig. 3M; Fig. 4G-H, J), and 400 pixels (Fig. S4D), where the circular region was placed with the center of circle aligned

with the center of the ectodermal tissue. Radial profiles were calculated on the entire stack for all replicates. To remove confounding signals measured from within the ectodermal tissue, a cutoff was established based on the Twist profile and removed from the dataset. The data were then recalibrated such that the x axis values represent distance from the edge of the ectoderm rather than the center of the circular ROI (Except for Fig. 1B). Radial intensity profiles of DAPI, Sox9, and Twist were normalized for Fig. 1B to show relative profiles for all channels on the same plot. For Fig. 3M, the radial intensity profile for the expected increase in Twist intensity at higher cell densities was produced by first measuring the average % increase in DAPI intensity as a function of distance from the ectoderm. These values were then multiplied to the Twist intensity profiles of each replicate. Each radial line intensity profile was integrated through an area under the curve (AUC) analysis in GraphPad Prism, which was calculated for all replicates across all conditions. These values were compared for statistical analyses (see Statistical Analysis).

Cell aspect ratios in the organite platform were measured in experiments where a low percentage (<5%) of equivalently-staged limb mesenchyme from GFP-labeled chicks were mixed in. Images were processed through thresholding and basic watershed transformation before individual GFP cells were identified through Analyze Particles where measurements like cell aspect ratio were made.

Analysis of DAPI, Sox9, Twist, and FN profiles in *ex vivo* assays were performed using Fiji (ImageJ, NIH). For Sox9 expression, background subtraction was performed on the Sox9 channel using a reference value calculated from the average mean gray intensity of 20–30 randomly selected nuclei in $Sox9^-$ regions. The background-subtracted images were converted into a binary mask via thresholding to measure the total $Sox9^+$ area. DAPI images were converted into a binary mask and measured for total nuclear area. The percentage of $Sox9^+$ area was calculated as: % $Sox9^+$ area = ($Sox9^+$ mask area / DAPI mask area) × 100. Since DAPI staining was consistent with high signal-to-noise ratios across samples, background subtraction was not applied to the DAPI channel. Twist intensity (Fig. S3E) was quantified by measuring integrated density following background subtraction using the same method as for Sox9. All values were normalized to the mean integrated density of the control group plated at 5,000 cells/μL. Twist/DAPI ratio (Fig. 3F) was calculated by dividing background-subtracted integrated density of Twist by the DAPI integrated density and normalized to the control group mean. Fibronectin intensity (Fig. 3D) was quantified by measuring the integrated density of the Fibronectin channel. Background subtraction was not applied as the fibronectin staining was consistent with high signal-to-noise ratios across samples. N-cadherin+ area (Fig. 3I) was measured from binary masks created from thresholding following background subtraction.

The histograms of fibronectin fiber orientations were generated with the Directionality FIJI plugin, utilizing Fourier component analysis on 200 x 400 pixel regions that were oriented parallel to the circumferential axis of the fibronectin ring. For Fig. 5E, the same ROIs used to produce the orientation histograms in Fig. 5D were also measured for mean FN intensities in ImageJ. For Fig. S5A, the comparison to the cartilage network outside of the ring was made with the same ROIs for rings but placed further within the cartilage tissue.

Statistical Analysis

See Supplementary Table S1 for full documentation of experimental trials and sample sizes. Statistical comparisons between two groups were performed using unpaired Mann–Whitney tests in GraphPad Prism. All tests were two-tailed and non-parametric. Error bars represent the standard deviation (SD), and exact p-values and sample sizes (n) are reported in the

figure legends. For radial intensity profile comparison across conditions, the area under the curve (AUC) of each replicate's profile was calculated and used as a single-value summary. A Kruskal–Wallis test was used to assess statistical significance across conditions.

Simulations

A mathematical model was designed to help evaluate some of our hypotheses regarding supracellular patterning. We constructed a nonlinear system of partial differential equations that represent the essential mechanical factors that we suspect are organizing both cells and matrix in our experiments. The full details of this model are presented in the Supplementary Text; however, we provide a brief summary of its structure here. The experimental system is represented as a series of continuum fields interacting in a bounded 2D domain (either a disk or an annulus). The patterning of cells is described by their density $c(x,t)$, which evolves via a combination of diffusion, haptotaxis, and cell-cell adhesion. The ECM is treated as a compressible viscoelastic fluid, characterized by its density $\rho(x,t)$, bulk pressure $p(x,t)$, and deviatoric stress $\boldsymbol{\sigma}$(x, t). Material is constantly added to the matrix in proportion to the local cell density, and cells likewise deform the matrix through active contractility. Finally, we characterize the feedback between cellular behavior and the supracellular environment by introducing two feedback variables $I(x,t)$ and $N(x,t)$, which represents the mean commitment of cells at (x,t) to cell-ECM or cell-cell interactions, respectively. We introduce mutual negative feedback between these two variables, leading cells to favor one or the other class of interaction in a way that is modulated by local cell and ECM density. These feedback variables are co-moving with the local cell population and so are also subject to advection and diffusion.

Supplementary Text

Additional details for mathematical model (see attached)

Supplemental Material: A continuum model for supracellular pattern formation in the limb

1 Introduction

This document describes a comprehensive mathematical model for tissue dynamics that couples cell density evolution, extracellular matrix (ECM) mechanics, cell feedback determination, and morphogen signaling. Ultimately, this is a minimal model that constitutes the simplest possible picture, containing what our experiments suggest are the key feedback mechanisms that determine cell activity. Before presenting the model, it is useful to establish some pre-existing theories of cell aggregation and patterning in the limb bud, providing context for our model. Three major mechanisms of spatial patterning have been investigated historically: 1) morphogen-based patterning via diffusion-driven Turing instabilities, 2) aggregation through differential cell adhesion, and 3) mechanically induced patterning via cell-ECM traction or taxis. Our experiments have led us to develop a model with elements of the second and third of these mechanisms [10].

Of particular relevance is the early mechanical pattern formation model proposed by Murray and Oster [6, 8]. These authors proposed a system of partial differential equations that features the interaction of a motile cell population with a passive extracellular matrix (ECM), which yields spontaneous symmetry breaking and pattern formation via mechanical instabilities. As described below, we adopt a variation on this modeling approach in our own consideration of cell-ECM interactions. At the same time, our model differs heavily this previous work in several regards: 1) we consider much greater variations in ECM density, and so must adopt different constitutive laws to account for this, 2) we include an n-cadherin linked cell-cell adhesion as an alternative mechanism of cell aggregation to cell-ECM interaction and a mutual repression based feedback to select between these mechanical modes, and 3) we consider the modulation of our mechanics by a morphogen field (namely Wnt).

For now, we neglect the role of long-range chemical signaling and consider dynamics as depending only on responses to local mechanical conditions. However, we note that considerable effort has been placed on examining such signaling in the limb [7]. A less parsimonious model of patterning in the limb would surely include morphogen-based signaling, but for our purposes, the cost of adding yet another patterning mechanism on top of the mechanical schemes discussed would surely render our model over-complex and uninterpretable. At the same time, we highlight that the agent-based models found in Ref. [3] and especially [5] share mechanistic similarities with our continuum model.

The remainder of this supplement is organized as follows. Section 2 outlines the key aspects of our model, providing commentary on specific assumptions and modeling choices. Section 3 describes the rescaling and non-dimensionalization of our problem. Section 4 then outlines our numerical scheme.

2 Governing Equations

2.1 Variables of interest

Our model is composed of the following functions over a bounded 2D spatial domain Ω. In the following sections, we define the equations of motion for these fields and explain our reasoning.

$c(\mathbf{x}, t)$	Cell density
$\mu(\mathbf{x}, t)$	Chemical potential
$\rho(\mathbf{x}, t)$	ECM density
$\mathbf{v}(\mathbf{x}, t)$	ECM velocity
$p(\mathbf{x}, t)$	ECM pressure field
$\boldsymbol{\sigma}(\mathbf{x}, t)$	ECM deviatoric stress
$I(\mathbf{x}, t)$	Integrin commitment
$N(\mathbf{x}, t)$	N-cadherin commitment
$W(\mathbf{x})$	Wnt morphogen concentration

2.2 Cell Density and Chemical Potential

Under our model, cells are treated as a conserved scalar field evolving through linear diffusion as well as several competing interactions. We choose to represent these interactions via an effective potential, μ, mainly for convenience and consistency with our FEM scheme, detailed below. We have two complementary interactions driving aggregation: a cell-cell adhesion based upon local cell density and mediated by our N-cadherin variable N, and a haptotaxis term based upon ECM density and mediated by the variable I. We also include a quadratic repulsive potential to represent short-range steric repulsions in crowded cell environments, and an additional spatial term penalizing interfaces, which is required to stabilize the problem against short-wavelength fluctuations. Our choice to neglect cell division follows from limited experimental evidence suggesting that cell proliferation plays a meaningful role on experimental timescales. Taken together, our equations of motion for the cell density are:

$$\frac{\partial c}{\partial t} = \nabla \cdot [c \nabla \mu] + D_c \nabla^2 c \tag{1}$$

where chemical potential is given by:

$$\mu = -\Lambda_{\text{interface}} \nabla^2 c - A_{\text{adhesion}} N c - A_{\text{taxis}} I \rho + B c^2 \tag{2}$$

and

- D_c is a cell diffusion rate
- A_{adhesion} is the cell-cell adhesion coefficient
- A_{taxis} is the taxis coefficient
- $\Lambda_{\text{interface}}$ is an interfacial energy cost
- B is a coefficient restricting cell crowding

As a comment, in the absence of ECM ($\rho = 0$), the long-timescale dynamics of this system reduces to a standard binoidal phase separation process between regions of high and low cell density.

2.3 ECM evolution

For the purposes of this model, we adopt a heavily simplified description of the extracellular matrix as an isotropic, passive viscoelastic fluid. We comment that this choice brings us simplicity and ease of interpretation, but the real ECM is a complex cross-linked network, and so we are surely sacrificing fidelity to the real constitutive law. Indeed, accurate coarse-grained theories of active cross-linked networks remain an open theoretical question that is beyond the scope of this paper [4]. At the same time, the present constitutive law proves effective for illustrating our experimental observations.

A key feature of our problem, in contrast to previous models of cell-ECM interaction [8], is the presence of large variations in matrix density. Consequently, we first introduce a scalar ECM density ρ which obeys a continuity equation:

$$\frac{\partial \rho}{\partial t} + \nabla \cdot (\rho \mathbf{v}) = K_b I c \tag{3}$$

In keeping with the experimental observation that total ECM quantity is monotonically increasing throughout our experiments, we introduce a cell-dependent matrix synthesis with rate K_b and intentionally exclude a degradation term. The consequence is that our system has no steady state behavior, except in the special case where the variable $Ic = 0$ everywhere. A force balance law establishes the ECM velocity v: the key stresses associated with this are a small baseline viscosity, a bulk elastic pressure p and shear stress $\boldsymbol{\sigma}$, and an isotropic active contractile stress:

$$\eta_0 \nabla^2 \mathbf{v} + \nabla p + \nabla \cdot \boldsymbol{\sigma} + \nabla(\Gamma I c) = 0 \tag{4}$$

Here,

- η_0 is a small basal ECM viscosity
- $\Gamma > 0$ is a cell-ECM traction parameter establishing a contractile active force

We assume an elastic component of our matrix obeys a Maxwell-type dynamics with bulk modulus K, shear modulus G, and relaxation timescale T_{relax}. As a consequence, we write our bulk pressure evolutions as

$$\frac{\partial p}{\partial t} = K_0 \rho \nabla \cdot \mathbf{v} - \frac{p}{T_{\text{relax}} \rho} \tag{5}$$

and the stress tensor as:

$$\frac{\partial \boldsymbol{\sigma}}{\partial t} = G_0 \rho \dot{\boldsymbol{\varepsilon}} - \frac{\boldsymbol{\sigma}}{T_{\text{relax}} \rho} \tag{6}$$

Here $\dot{\boldsymbol{\varepsilon}} = \frac{1}{2}\left(\nabla v + \nabla v^T\right)$. We note that we adopt a density dependence in this constitutive relation, which is necessary to account for density-induced stiffening in our system. Note that density both increases the elastic moduli and simultaneously increases the stress relaxation time scales: a dense ECM is thus both stiffer and more solid in our model.

2.4 Cell Behavior Dynamics

An essential feature of our model is the mutually inhibitory feedback between cell-cell and cell-ecm modes. We adopt a simple picture of this mechanism by imagining that an individual cell has only a finite amount of cytoskeletal machinery to devote to mechanical activity. To capture this, we treat the variables I and N as a measure of what fraction of their resources local cells are devoting to focal-adhesion or n-cadherin-related activities. We represent the tradeoff between these

two strategies as a local bistable switch based on mutual inhibition: commitment to one strategy represses commitment to the other. The degree of this mutual repression is designed to replicate local responsiveness of cells to their supracellular environment: high ECM density will weaken the repression of cell-ECM interactions, and both high cell density and high Wnt exposure will weaken the repression of cell-cell adhesion. It is worth noting that cell transport must be properly accounted for: we expect our feedback dynamics to occur in a co-moving frame with individual cells, rather than in the Eulerian lab frame (a more detailed explanation of this phenomenon can be found in Ref. [9]). As a result, we supplement our local kinetic terms with transport terms that represent the net motion of the cell population and internal mixing due to diffusion. Our resulting equations of motion are:

$$\frac{\partial I}{\partial t} = D_c \nabla^2 I - \mathbf{v}_c \cdot \boldsymbol{\nabla} I + K_{feedback} \left[\frac{\rho}{\rho + \Theta_{ecm} N^2} - I \right] \tag{7}$$

and

$$\frac{\partial N}{\partial t} = D_c \nabla^2 N - \mathbf{v}_c \cdot \boldsymbol{\nabla} N + K_{feedback} \left[\frac{c + k_w W}{c + k_w W + \Theta_{cell} I^2} - N \right] \tag{8}$$

where:

- $K_{feedback}$ is the feedback switching rate
- Θ_{ecm} is the ECM threshold parameter
- Θ_{cell} is the cell threshold parameter
- $\mathbf{v}_c = -\nabla \mu - D_c \nabla \log c$ is the density normalized cell flux
- k_w governs Wnt sensitivity

2.5 Wnt Morphogen Field

The Wnt concentration satisfies a reaction-diffusion equation:

$$-k_w W + D_w \nabla^2 W + S_W = 0 \tag{9}$$

where L is the Wnt length scale parameter and S_W is a global source term. We supplement this in the organite simulations with an inner boundary condition:

$$W + L_W^2 \nabla W \cdot \hat{n} + S_{\text{ect}} = 0 \tag{10}$$

With this being said, without our micromass simulations, we treat S_W as a uniform source term and set it to zero in the other simulations.

3 Rescaling

We adopt the following set of rescalings in order to simplify our mathematical description. First, we introduce these characteristic scales:

Cell density	c_0	$\sqrt{\frac{D_c}{b}}$
Length	L_0	$\left(\frac{\Lambda_{\text{interface}}}{D_c b}\right)^{1/4}$
Time	T_0	$\left(\frac{\Lambda^2_{\text{interface}}}{D_c^3 b}\right)^{1/2}$
ECM density	ρ_0	$\left(\frac{\Lambda^2_{\text{interface}}}{D_c^3 b T^2_{\text{relax}}}\right)^{1/2}$
Stress	σ_0	$\frac{K}{T^2_{\text{relax}}}\left(\frac{\Lambda^2_{\text{interface}}}{D_c^3 b}\right)^{1/2}$
Wnt	w_0	$\frac{1}{k_w}\left(\frac{\Lambda^2_{\text{interface}}}{D_c^3 b T^2_{\text{relax}}}\right)^{1/2}$

3.1 Complete System

The complete system of governing equations post-rescaling is:

$$\frac{\partial c}{\partial t} = \nabla \cdot (c \nabla \mu) + \nabla^2 c \tag{11}$$

$$\mu = -\nabla^2 c - \Delta N c - \tau I \rho + c^2 \tag{12}$$

$$\frac{\partial \rho}{\partial t} + \nabla \cdot (\rho \mathbf{v}) = k_b I c \tag{13}$$

$$\eta \nabla^2 \mathbf{v} + \nabla p + \nabla \cdot \boldsymbol{\sigma} + \nabla(\gamma I c) = 0 \tag{14}$$

$$\frac{\partial p}{\partial t} = \rho \nabla \cdot \mathbf{v} - \frac{p}{\rho} \tag{15}$$

$$\frac{\partial \boldsymbol{\sigma}}{\partial t} = G \rho \dot{\boldsymbol{\varepsilon}} - \frac{\boldsymbol{\sigma}}{\rho} \tag{16}$$

$$\frac{\partial I}{\partial t} = \nabla^2 I - \mathbf{v}_c \cdot \boldsymbol{\nabla} I + k_{feedback}\left[\frac{\rho}{\rho + \theta_{ecm} N^2} - I\right] \tag{17}$$

$$\frac{\partial N}{\partial t} = \nabla^2 N - \mathbf{v}_c \cdot \boldsymbol{\nabla} N + k_{feedback}\left[\frac{c + W}{c + W + \theta_{cell} I^2} - N\right] \tag{18}$$

$$-W + L^2 \nabla^2 W = S_W \tag{19}$$

3.2 Boundary Conditions

The boundary conditions for the system are:

$$\nabla c \cdot \mathbf{n} = 0 \quad \text{on } \partial\Omega \tag{20}$$

$$\nabla \mu \cdot \mathbf{n} = 0 \quad \text{on } \partial\Omega \tag{21}$$

$$\nabla \rho \cdot \mathbf{n} = 0 \quad \text{on } \partial\Omega \tag{22}$$

$$\mathbf{v} = \mathbf{0} \quad \text{on } \partial\Omega \tag{23}$$

$$\nabla I \cdot \mathbf{n} = 0 \quad \text{on } \partial\Omega \tag{24}$$

$$\nabla N \cdot \mathbf{n} = 0 \quad \text{on } \partial\Omega \tag{25}$$

$$L^2 \nabla W \cdot \mathbf{n} = S_{\text{ect}} \tag{26}$$

We note that W_{boundary} is a function defined on the domain boundary. In micro-mass type simulations, this equals zero. In organite-based simulations, it is zero on the outer boundary of the annulus, and equal to a constant W_b on the inner boundary.

3.3 Initial Conditions

The initial conditions are specified as:

$$c(\mathbf{x}, 0) = c_{init} + \mathcal{N}(0, \sigma^2) \tag{27}$$
$$\mu(\mathbf{x}, 0) = 0 \tag{28}$$
$$\rho(\mathbf{x}, 0) = \rho_{init} \tag{29}$$
$$\mathbf{v}(\mathbf{x}, 0) = \mathbf{0} \tag{30}$$
$$p(\mathbf{x}, 0) = 0 \tag{31}$$
$$\boldsymbol{\sigma}(\mathbf{x}, 0) = \mathbf{0} \tag{32}$$
$$I(\mathbf{x}, 0) = 0.5 + \mathcal{N}(0, 10^{-2}) \tag{33}$$
$$N(\mathbf{x}, 0) = 0.5 + \mathcal{N}(0, 10^{-2}) \tag{34}$$
$$W(\mathbf{x}, 0) = 0 \tag{35}$$

where $\mathcal{N}(0, \sigma^2)$ represents Gaussian noise with mean 0 and standard deviation σ.

3.4 Parameter choices

Symbol	Meaning	Value (Inverted)	Value (Micromass)	Value (Organite)
Δ	Cell-cell adhesion coefficient	5.0	3.0	5.0
τ	Haptotaxis strength coefficient	0.05	0.0	0.0
η	ECM base viscosity	0.01	1.0	0.01
γ	Cell traction	0.5	10.0	0.65
k_b	ECM synthesis rate	2.5	2.5	2.5
G	Shear modulus	$\frac{1}{9}$	$\frac{1}{9}$	$\frac{1}{9}$
$k_{feedback}$	Cell feedback rate	100.0	100.0	20.0
θ_{ecm}	Cell-ECM threshold	1.25	0.05	1.25
θ_{cell}	Cell-cell threshold	1.8	0.5	1.8
L_w	Wnt diffusion length scale	0.5	N/A	0.25
ρ_i	Initial ECM density	0.05	0.005	0.05
c_i	Base cell density	0.3	0.6	0.3
S_{ect}	Ectodermal boundary wnt	5.0	0	5.0
S_W	Bulk Wnt dosage	0.0	0.825	0.0

Table 1: Baseline parameter values

Here, we briefly discuss our choice of parameters. Experimental concerns limit our ability to directly measure many of the key mechanical constants of the system, but in some cases, we were able to constrain ourselves based on known results. The dimensionless shear modulus was chosen under the assumption that the ECM, though compressible, possesses a fairly large Poisson ratio (≈ 0.8), and the base viscosity was set to be a fairly small effect - it was primarily added to the model for numerical stability benefits. Likewise, the diffusion length scale of Wnt was selected to ensure a tight localization relative to the cell aggregate size. Similarly, the parameters Δ, τ, and γ were chosen so that our simulations would be within the spontaneous pattern formation regime. Finally, we tuned the threshold parameters θ_i so that the feedback mechanism reached the bistable regime we desired. We also note that differing plating and other experimental conditions between the micromass, inverted, and organite experiments led us to select different parameters for their control simulations.

4 Numerical Implementation Notes

The spatial discretization uses first-order finite elements for all fields. The implementation uses the Dolfinx FEM library with PETSc linear solvers [2, 1]. Time integration is performed using a first-order semi-implicit scheme described below, with fixed timestep $\Delta t = 1 \times 10^{-3}$.

4.1 Weak Form Finite Element Discretization

The weak form time stepping scheme uses a semi-implicit treatment where linear terms are implicit and nonlinear terms are explicit. We have split our timestepping problem into several matrix blocks, which are solved in sequence: within each block, we employ a mixed finite element formulation and solve the resulting linear problems using LU-factorization. We outline the weak form of the scheme below, using the notation $(\cdot,\cdot)$ for the L^2 inner product over the domain Ω and $(\cdot,\cdot)_{\partial Omega}$ for the product integral over the boundary. We introduce $\phi_c, \phi_\mu, \phi_\rho, \phi_v, \phi_p, \phi_\sigma, \phi_I, \phi_N$ as test functions from the appropriate first-order Lagrange finite element spaces.

Cell density and chemical potential system:

$$\begin{aligned}(c^{N+1},\phi_c) - \Delta t\left[(\nabla\mu^{N+1},\nabla\phi_c) + (\nabla c^{N+1},\nabla\phi_c)\right] &= (c^N,\phi_c) + \Delta t((1-c^N)\nabla\mu^N,\nabla\phi_c)\\ (\mu^{N+1},\phi_\mu) + (\nabla c^{N+1},\nabla\phi_\mu) &= -(\Delta N^N c^N,\phi_\mu) - (\tau I^N\rho^N,\phi_\mu) + ((c^N)^2,\phi_\mu)\end{aligned}$$

We note that this scheme introduces a small artificial viscosity of order Δt in our time evolution for c, which helps stabilize the code against strong advective fluxes at a small cost to accuracy.

ECM system:

$$\begin{aligned}(\rho^{N+1},\phi_\rho) &= (\rho^N,\phi_\rho) - \Delta t(v^N\rho^N,\nabla\phi_\rho) + \Delta t(k_b I^N c^N,\phi_\rho)\\ -\eta(\nabla v^{N+1},\nabla\phi_v) + (\nabla p^{N+1},\phi_v) + (\nabla\cdot\sigma^{N+1},\phi_v) + \eta(w_{dir}v^{N+1} + \nabla v^{N+1}\cdot\hat{n},\phi_v)_{\partial\Omega} &= -(\nabla(\gamma I^N c^N),\phi_v)\\ (p^{N+1},\phi_p) &= (p^N,\phi_p) + \Delta t(\rho^N\nabla\cdot v^N,\phi_p) - \Delta t(p^N/\rho^N,\phi_p)\\ (\sigma^{N+1},\phi_\sigma) &= (\sigma^N,\phi_\sigma) + \Delta t G(\rho^N\dot{\varepsilon}^N,\phi_\sigma) - \Delta t(\sigma^N/\rho^N,\phi_\sigma)\end{aligned}$$

We have chosen a weak formulation of the Dirichlet boundary on v, with a penalty weight $w_{dir} = 10^3$.

Feedback system:

$$\begin{aligned}(I^{N+1},\phi_I) + \Delta t(\nabla I^{N+1},\nabla\phi_I) &= (I^N,\phi_I) + \Delta t(\nabla\mu^N,\nabla I^N)\phi_I\\ &\quad + \Delta t(\nabla I^N\cdot\nabla c^N/c^N,\phi_I) + \Delta t k_{feedback}\left(\frac{1}{1+\frac{\theta_{ecm}}{\rho^N}(N^N)^2} - I^N,\phi_I\right)\\ (N^{N+1},\phi_N) + \Delta t(\nabla N^{N+1},\nabla\phi_N) &= (N^N,\phi_N) + \Delta t(\nabla\mu^N,\nabla N^N)\phi_N\\ &\quad + \Delta t(\nabla N^N\cdot\nabla c^N/c^N,\phi_N) + \Delta t k_{feedback}\left(\frac{1}{1+\frac{\theta_{cell}}{c^N+W^N}(I^N)^2} - N^N,\phi_N\right)\end{aligned}$$

Wnt system:

$$-(L_w^2\nabla W,\nabla\phi_W) - (W,\phi_W) = -(S_W,\phi_W) - (S_{\text{ect}},\phi_W)_{\partial\Omega}$$

4.2 Simulation domains

All simulations were performed on unstructured triangulated meshes. In cases where we replicate the micromass dynamics, we employ a disk-shaped mesh of radius $R = 8$ with characteristic edge length $\Delta x = 0.2$. In the organite simulations, we use an annular domain with outer radius $R_{\text{out}} = 5$ and $R_{\text{in}} = 0.25$ with $\Delta x = 0.1$. Finally, in our 'right-side-out' example, we use a disk of radius $R = 5$ and $\Delta x = 0.1$.

References

[1] Balay, S., Abhyankar, S., Adams, M., Brown, J., Brune, P., Buschelman, K., Dalcin, L., Dener, A., Eijkhout, V., Gropp, W., et al. Petsc users manual. (2019).

[2] Baratta, I. A., Dean, J. P., Dokken, J. S., Habera, M., HALE, J., Richardson, C. N., Rognes, M. E., Scroggs, M. W., Sime, N., & Wells, G. N. Dolfinx: the next generation fenics problem solving environment. (2023).

[3] Christley, S., Alber, M. S., & Newman, S. A. Patterns of mesenchymal condensation in a multiscale, discrete stochastic model. *PLoS computational biology* **3**, e76, (2007).

[4] Fürthauer, S., Needleman, D. J., & Shelley, M. J. A design framework for actively crosslinked filament networks. *New Journal of Physics* **23**, 013012, (2021).

[5] Kiskowski, M. A., Alber, M. S., Thomas, G. L., Glazier, J. A., Bronstein, N. B., Pu, J., & Newman, S. A. Interplay between activator–inhibitor coupling and cell-matrix adhesion in a cellular automaton model for chondrogenic patterning. *Developmental Biology* **271**, 372–387, (2004).

[6] Murray, J. D. & Oster, G. F. Cell traction models for generating pattern and form in morphogenesis. *Journal of mathematical biology* **19**, 265–279, (1984).

[7] Newman, S. A. & Frisch, H. Dynamics of skeletal pattern formation in developing chick limb. *Science* **205**, 662–668, (1979).

[8] Oster, G. F., Murray, J. D., & Harris, A. Mechanical aspects of mesenchymal morphogenesis. *Development* **78**, 83–125, (1983).

[9] Plum, A. M. & Serra, M. Morphogen patterning in dynamic tissues. *bioRxiv*, 2025–01, (2025).

[10] Zhang, Y.-T., Alber, M. S., & Newman, S. A. Mathematical modeling of vertebrate limb development. *Mathematical biosciences* **243**, 1–17, (2013).

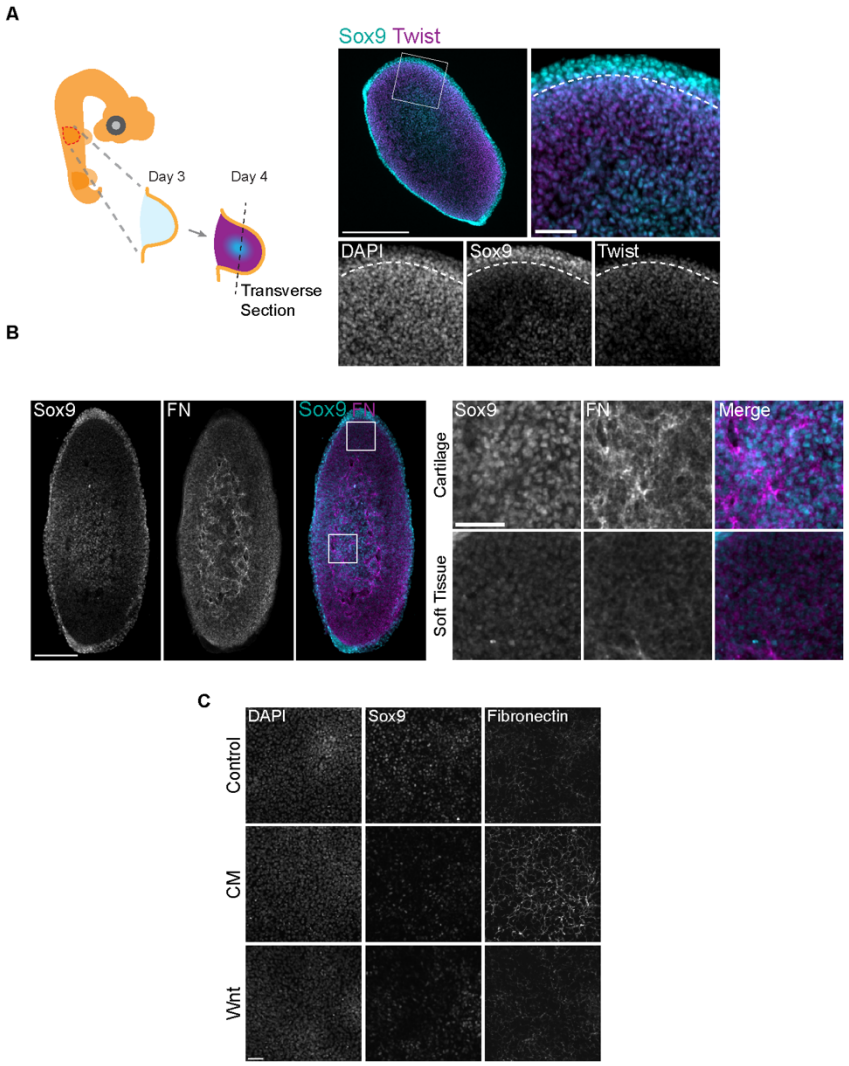

Supplemental Figure S1. (A) Left, Schematic showing approximate orientation of transverse sections through limb buds. Right, transverse sections of E4.5 limb buds stained for DAPI, Sox9, and Twist. Dashed lines are drawn at the boundary between the ectoderm (which is Sox9+) and mesenchyme. Mesenchymal cells are more closely packed near the ectoderm. Scale bar, 300 µm (whole bud)). **(B)** Sections of E4.5 limb buds stained for Sox9 and FN showing FN network in the core of the limb bud where Sox9 is expressed and cartilage forms. Scale bar, 150 µm (whole bud) . **(C)** DAPI, Sox9, and FN in *ex vivo* cultures treated with ectoderm-conditioned media (CM) (see Methods) show increased FN in CM-treated cultures. Scale bars = 50 µm unless otherwise noted.

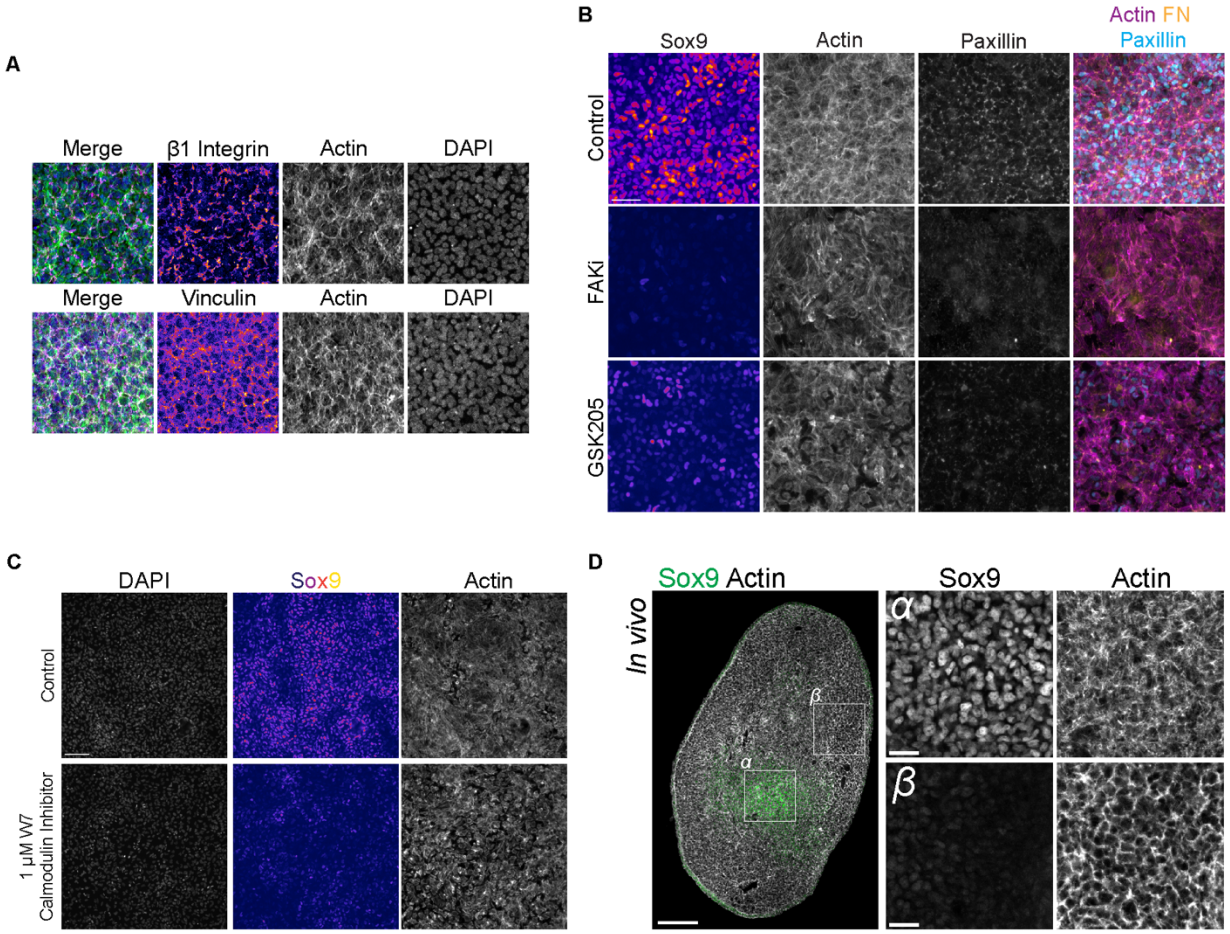

Supplemental Figure S2. (A) DAPI, Actin, β1 integrin, and Vinculin in *ex vivo* cultures. Scale bar, 50 μm. **(B)** Sox9, Actin, and Paxillin in *ex vivo* cultures plated in a suspension of 3 mg/mL Matrigel and treated with 10 μM FAKi or 50 μM GSK205 to minimize cell loss in these treatment conditions. Scale bar, 50 μm. **(C)** DAPI, Sox9, and Actin in *ex vivo* cultures grown in Matrigel treated with 1 μM W7 (calmodulin inhibitor) show similar reductions as TRPV4 channel activity inhibition. Scale bar, 100 μm. **(D)** E5 limb bud section stained for DAPI, Sox9, and Actin shows a pattern of more diffuse actin fibers in Sox9-positive cells as compared to Sox9-negative cells. Scale bars, 150 μm (left) and 20 μm (right cropped images).

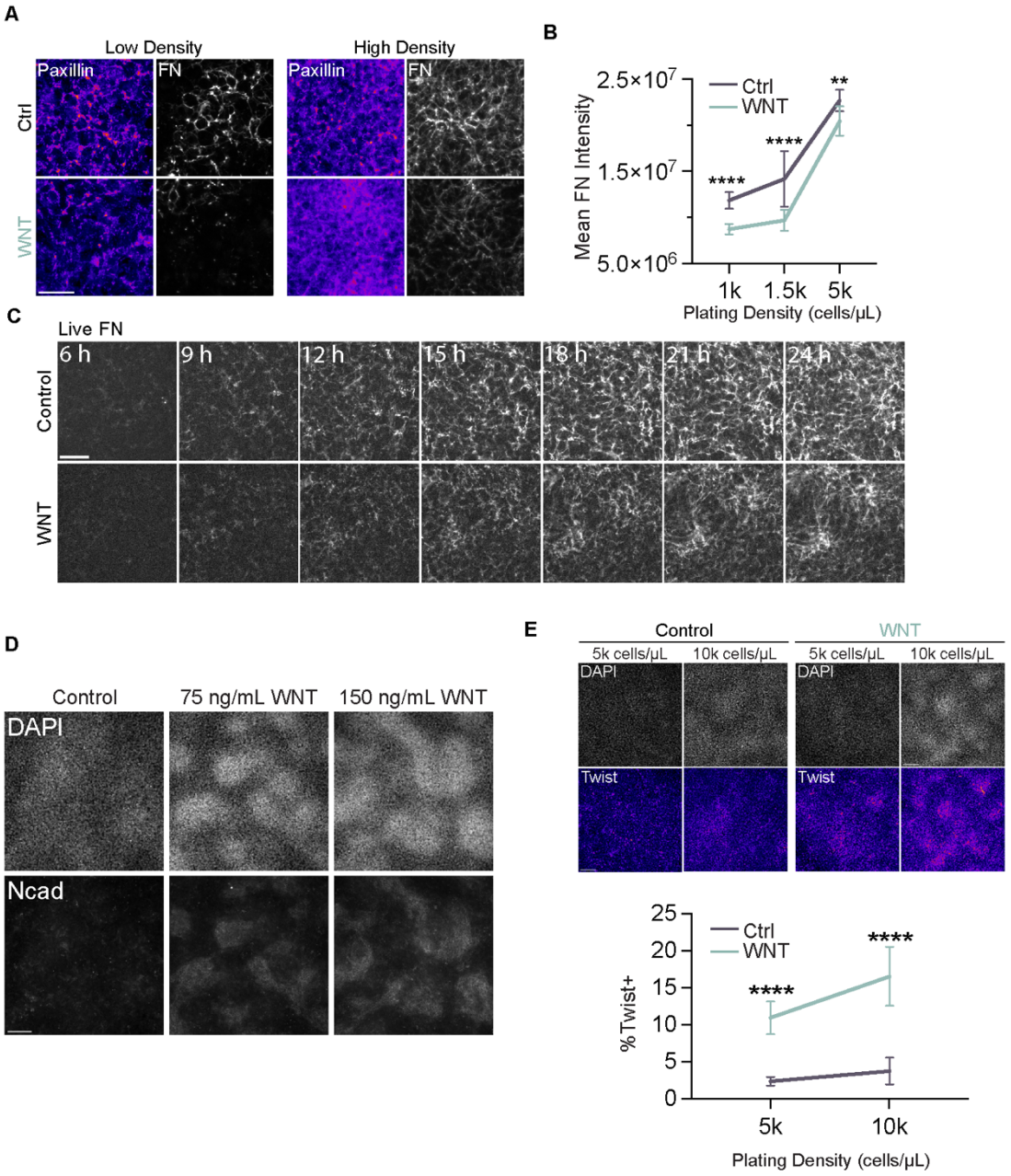

Supplemental Figure S3. (A) Paxillin and FN in control and Wnt-treated *ex vivo* cultures at low (5,000 cells/µL) or high (10,000 cells/µL) densities. Scale bar, 50 µm. **(B)** Mean FN intensity comparison of S3A. **** $p < .0001$; ** $p = .0055$. **(C)** Montage from live imaging of FN in high density control and Wnt-treated *ex vivo* cultures (Movie S5). Scale bar, 50 µm. **(D)** *Ex vivo* cultures treated with 75 or 150 ng/mL Wnt stained for DAPI and Ncad show Wnt induces Ncad in a dose-dependent manner. Scale bar, 100 µm. (**E**) Top, Twist in control and Wnt-treated *ex vivo* cultures of different cell densities. Twist is activated in more densely packed aggregates. Scale bar, 100 µm. Bottom, Quantification of %Twist+ area. **** $p < .0001$; *** $p = .0005$.

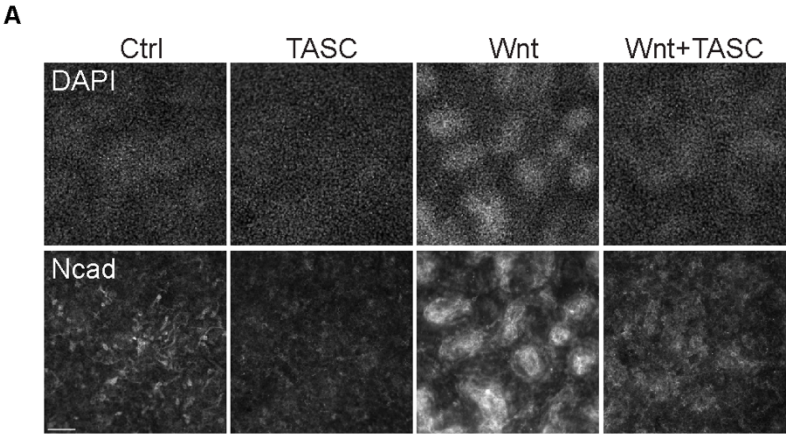

Supplemental Figure S4. (A) DAPI and Ncad in control or Wnt-treated *ex vivo* cultures of limb progenitors with β1 integrin activation (TASC, 20 μg/mL) show decreased Ncad when cell-ECM engagement is increased. Scale bar, 100 μm.

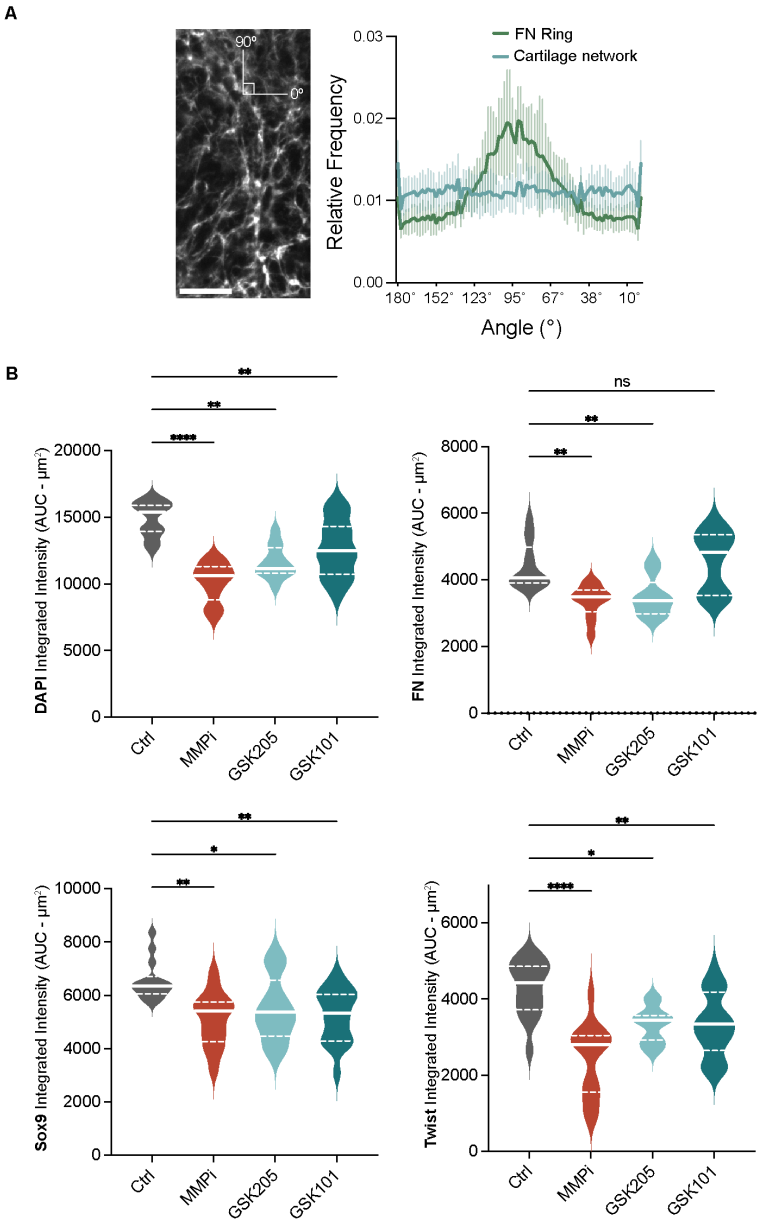

Supplemental Figure S5. (A) Histogram of FN fiber orientation in the FN boundary compared to the non-boundary areas of cartilage. Fiber orientations were measured with the boundary's circumferential axis parallel to 90° (see left image). Mean ± SD shown. Scale bar, 25 µm. **(B)** Comparison of integrated intensities through an area under the curve (AUC) analysis of plots in 5C shows significant decreases in soft tissue cell density and Twist expression in all treatment conditions. For comparisons to control for each signal: DAPI: **** $p < .0001$; ** $p = .0010$ (GSK205); ** $p = .0095$ (GSK101). FN: ** $p = .0038$ (MMPi); ** $p = .0097$ (GSK205); ns, not significant. Sox9: ** $p = .0014$ (MMPi); ** $p = .0034$ (GSK101); * $p = .0330$ (GSK205). Twist: **** $p < .0001$; ** $p = .0071$; * $p = .0233$.

Movie S1. Low ECM in the soft tissue of the organite system emerges through a dynamic remodeling process.
Organites (20,000 cells/µL) were cultured with AF488-conjugated FN antibodies on a Zeiss CD7. Movies are run at 21 fps. Time stamps are displayed as hours:minutes. Scale bar, 100 µm.

Movie S2. Clearing of FN associated with outwards "flow" of fibers away from the ectoderm.
Organites (20,000 cells/µL) were cultured with AF488-conjugated FN antibodies on a Zeiss CD7. Movies are run at 21 fps. Time stamps are displayed as hours:minutes. Scale bar, 100 µm.

Movie S3. Fibronectin (FN) increases in density to form a dense network in limb progenitor *ex vivo* cultures.
Ex vivo cultures treated with AF488-conjugated FN antibodies (FN-3) imaged on a Zeiss CD7. Movies are run at 21 fps. Time stamps are displayed as hours:minutes. Scale bar, 100 µm.

Movie S4. FN network dynamics in low density *ex vivo* cultures treated with Wnt.
Low density (5,000 cells/µL) *ex vivo* cultures treated with Wnt and AF488-conjugated FN antibodies imaged on a Zeiss CD7. Movies are run at 21 fps. Time stamps are displayed as hours:minutes. Scale bar, 100 µm.

Movie S5. FN network dynamics in high density *ex vivo* cultures treated with Wnt.
High density (10,000 cells/µL) *ex vivo* cultures treated with Wnt and AF488-conjugated FN antibodies imaged on a Zeiss CD7. Movies are run at 21 fps. Time stamps are displayed as hours:minutes. Scale bar, 100 µm.

Table S1. Statistical Values

Experiment/Figure	Trials	Total n analyzed
Fig. 1B (organite radial intensity profile)	5	12
Fig. 1D (cell aspect ratios)	2	78 cartilage cells, 65 soft tissue cells
Fig. 1F (FN orientation)	7	17 ring measurements, 21 non-ring measurements
Fig. 2A	3	8 per time point
Fig. 2B	3	23 for 1k cells/ µL, 20 for 1.5k cells/ µL, 16 for 5k cells/ µL
Fig. 2C (FN intensity from live movies)	2	10
Fig. 2E	3	32 control, 40 FAKi
Fig. 2F (Sox9 levels)	2	10 control, 9 FAKi, 6 GSK205, 6 GSK205+FAKi
Fig. 2H (Y27632 treatment)	2	24 control, 20 Y27632 treatment
Fig. 2I (Y27632 rescue of GSK205)	2	20 control, 28 GSK205, 17 Y27632, 15 Y27632+GSK205
Fig. 3B (GSK101 rescue of WNT)	2	24 for control, 16 for WNT, 24 for WNT+GSK101
Fig. 3D (Exogeneous FN supplement to control and Wnt micromasses)	2	12 for each conditions (control-control, control-FN, WNT-control, WNT-FN)
Fig. 3F (Wnt and ADH-1 treatment to micromasses)	3	8 per condition
Fig. 3I (N-cadherin expression across density with control and WNT treatment)	2	4 for control at 2k cells/ µL, 8 for all other conditions (control at 4k cells/ µL, 8 for control at 8k cells/ µL, WNT at 2k cells/ µL, WNT at 4k cells/ µL, 8 for WNT at 8k cells/ µL)
Fig. 3K (Density gradient with WNT treatment)	3	23 control at 1k cells/ µL, 20 control at 1.5k cells/ µL, 12 control at 5k cells/uL. 23 WNT-treated at 1k cells/ µL, 16 WNT-treated at 1.5k cells/ µL, 12 WNT-treated at 5k cells/uL.
Fig. 3M (Twist intensity comparing low vs. high density organite)	3	8 low density, 9 high density
Fig. 4E (Ncad levels after TASC treatment)	4	21 per condition
Fig. 5D (IWP treatment)	2	15 control, 12 IWP
Fig. 5F (IWP treatment)	5	16 control, 16 IWP
Fig. 6 and S5	7	16 control, 15 MMPi, 11 GSK205, 20 GSK101